Three-Dimensional Oxygen Concentration Monitoring in Hydrogels Using Low-Cost Phosphorescence Lifetime Imaging for Tissue Engineering

Three-Dimensional Oxygen Concentration Monitoring in Hydrogels Using Low-Cost Phosphorescence Lifetime Imaging for Tissue Engineering

By XU MEI

B. Eng. (Huazhong University of Science and Technology, Wuhan, P. R. China)

A Thesis Submitted to the School of Graduate Studies in Partial Fulfilment of the Requirements for the Degree Master of Applied Science

McMaster University	MASTER OF APPLIED SCIENCE (2024)
Hamilton, Ontario, Canada	Biomedical Engineering
TITLE:	Three-Dimensional Oxygen Concentration Monitoring in Hydrogels Using Low-Cost Phosphorescence Lifetime Imaging for Tissue Engineering
AUTHOR:	XU MEI, B. Eng.
Supervisor	Dr. P. R. Selvaganapathy
NUMBER OF PAGES	xiv, 71

ABSTRACT

Oxygen concentration measurement in 3D hydrogels is vital in 3D cell culture and tissue engineering. However, standard 3D imaging systems capable of measuring oxygen concentration with adequate precision are based on advanced microscopy platforms which are not accessible in many laboratories due to the system's complexity and the high price. In this work, we present a fast and low-cost phosphorescence lifetime imaging design for measuring the lifetime of oxygen-quenched phosphorescence emission with 0.25 μs temporal precision and sub-millimeter spatial resolution in 3D. By combining light-sheet illumination and the frequency-domain lifetime measurement using a commercial rolling-shutter CMOS camera in the structure of a conventional optical microscope, this design is highly customizable to accommodate application-specific research needs, while also being low-cost as compared to advanced instruments. As a demonstration, we made a fluidic device with a gas-permeable film to create an artificial oxygen gradient in the hydrogel sample. Dye-embedded beads were distributed in the hydrogel to conduct continuous emission lifetime monitoring when nitrogen was pumped through the fluidic channel and changed oxygen distribution in the sample. The dynamics of the changes in lifetime co-related with their location in the gel of size 0.5 mm×1.5 mm×700 μm demonstrate the ability of this design to measure the oxygen concentration stably and precisely in 3D samples.

ACKNOLEDGEMENT

I extend my deepest gratitude to my esteemed supervisor Professor Ponnambalam Ravi Selvaganapathy, for his unwavering support and kindness throughout my master’s years. Prof. Selvaganapathy’s guidance was invaluable, as he consistently shared his remarkable ideas and experiences, offering profound insights when I encountered challenges in my research. His encouragement to explore various concepts and his provision of all necessary resources empowered me to implement my ideas effectively. The lessons I have learned under his mentorship will undoubtedly shape my approach to future challenges. I am truly fortunate to have had such a mentor who has played a pivotal role in my academic journey.

I would like to thank Dr. Qiyin Fang for his generous guidance since I was a visiting student at McMaster. He also offered precious help on my thesis and offered me opportunities to gain hands-on experience along the way. My appreciation also goes to all the committee members: Dr. Changqing Xu, Dr. Qiyin Fang, Dr. P. Ravi Selvaganapathy for their support and suggestions on my project.

I thank all my fellow labmates in the Center for Advanced Micro-Electro-Fluidics laboratory. Dr. Nidhi Jain has consistently been a supportive presence, never hesitating to offer her assistance both within and outside the lab. Vinay and Sreekant, whom I consider as big brothers, showed me everything I needed to know in the lab when I was a freshman. The success of my work owes much to the invaluable contributions of Aydin, Maedeh, Shadi, Neda, Mehraneh, and Sneha. Their expertise and unwavering commitment to aiding with my experiments played a pivotal role. I extend my sincere appreciation to each one of them for their selfless assistance.

Last but not least, I would like to deeply thank my parents and all my friends. It is their endless love that makes me go this far. This thesis is dedicated to them for their unconditional love for me.

TABLE OF CONTENTS

LIST OF FIGURES

LIST OF ALL ABBREVIATIONS

FLIM	Fluorescence lifetime imaging microscopy
TCSPC	Time-correlated single photon counting
TGSPC	Time-gated single photon counting
CMOS	Complementary metal-oxide-semiconductor
CCD	Charge-coupled device
PMT	Photomultiplier tube
SPAD	Single-photon avalanche diode
TDC	Time-to-digital converter
ICT	Intramolecular charge transfer
PtTFPP	Platinum(II)-5,10,15,20-tetrakis-(2,3,4,5,6-pentafluorphenyl)-porphyrin
PS	Polystyrene
PCL	Polycaprolactone
DCM	Dichloromethane

Chapter 1: Motivation and Organization

1.1 Motivation

Oxygen concentration is a crucial factor in a variety of biological research fields. In cell culture models, achieving an effective oxygen supply mechanism is often critical for the successful growth of cells, whether in laboratory culture dishes [1, 2] or industrial-level large-scale cell-culture reactors [3]. Furthermore, variations in oxygen levels in the cellular microenvironment are prevalent in both natural as well as engineered cell cultures. These alterations in oxygen tension are recognized for their role in regulating signaling cascades, ultimately resulting in metabolic and phenotypic changes [4]. Low oxygen tension, or hypoxia, is essential for many normal cellular processes like stem cell recruitment, proliferation, or differentiation [5]. In tumors, hypoxia leads to dysfunctional vascularization and alters cell metabolism, affecting tumorigenesis and angiogenesis [6, 7].

Controlling oxygen level in the microenvironment of cell cultures is thus desired for investigating the underlying cellular mechanisms at the tissue level, as well as to control the product quality in biofabrication to modulate the oxygen supply for optimal cellular growth. Numerous research studies have proposed designs capable of fine-tuning oxygen tension within the culture based on microfluidic devices [4, 8] or flow-controlled chambers [9]. Consequently, the demand for precise three-dimensional measurements of oxygen level in the microenvironment emerges not only with the development of devices focused on oxygen tension fine-tuning and other microfluidics [10, 11] but also in typical tissue constructs [12, 13]. To accommodate the millimeter-size dimensions of typical tissue constructs, optical imaging methods to measure the oxygen tension are usually favored over Clark electrodes as they are non-invasive, do not consume oxygen in the samples to achieve the sensing, and provide better accuracy and resolution [14]. Within these optical methods, quantifying the oxygen's quenching effect on the luminescence is decreased when the excited-state luminophore is deactivated upon contact with the oxygen molecule in the surrounding environment. Both intensity [15] and lifetime [8] of the luminescence can change due to quenching and these attenuations in the luminescence can be assessed to quantify oxygen concentration.

While the results from lifetime measurements are preferred as it is not affected by signal attenuations along various optical paths in the samples, the lifetime measurement procedures themselves, however, require considerable expertise and specialized equipment to measure the rapid temporal dynamics of luminescent processes, whose timescales range from nanoseconds to microseconds. Typically, sensitive and high-precision imaging systems like confocal and multiphoton laser scanning microscopes that are very expensive are used and offer gold-standard results, exhibiting capabilities to resolve nanosecond-level fluorescence lifetime and micrometer-scale spatial distribution of oxygen [16-20]. However, the high cost, system complexity, and complicated requirements for the sample preparation hinder their field application in tissue engineering. More recently, several research designs utilizing optical detectors in combination with customized optics have been built for oxygen monitoring in their specific cell culture constructs. Most of them conduct point measurements inside microfluidic chambers or culture mediums by placing the luminescent probes at fixed positions and adjusting the illumination and detector accordingly [21-24]. However, such configurations exhibit low spatial resolution and cannot provide sufficient information to map cellular metabolism with oxygen concentration in 3D. In other studies, 2D/3D oxygen mappings are proposed but still constructed with high-priced and advanced scientific cameras or fluorometers [25-27]. These instruments are designed with a large temporal dynamic range. Nevertheless, since most oxygen-indicating dyes have lifetimes in the range of microseconds, their high capabilities may be redundant and can lead to unnecessary costs. There are also previous studies that have demonstrated the utilization of conventional CCD devices for high temporal resolution measurements. This has been achieved through either low-level hardware control [28, 29] or the incorporation of image intensifiers to enable single photon counting [30, 31].

In this thesis, a cost-effective luminescence lifetime measurement design is proposed, combining the rolling-shutter mode CMOS-camera-based lifetime measurement with polymer microbeads that localize luminescence distributed throughout the 3D hydrogel culture construct when illuminated by a light sheet to determine the normoxic to hypoxic oxygen concentration in 3D with a sub-millimeter resolution. This design can be easily adapted to customized sample geometries, making it effective in various biological settings, aiming for fast prototyping with minimal efforts. The overall cost of all the system components could be as low as 1500 USD, significantly lower than oxygen imaging solutions using advanced instruments while maintaining competitive performance. This thesis also provides several experiment designs to validate the efficacy of the system based on artificial millimeter-scale oxygen gradient generated in a fluidic device.

1.2 Organization

This thesis is organized as follows:

Chapter 2 offers a comprehensive overview of the principles and contemporary methodologies employed in optical sensing of oxygen concentration, focusing on the luminescence quenching effect. Subsequently, the chapter presents a range of instruments and measuring strategies dedicated to luminescence lifetime, emphasizing its heightened reliability as an indicator of luminescence quenching. Finally, it briefly discusses the effectiveness of the conventional luminescence probe crafted from dye-embedded polymer structures.

Chapter 3 describes the methodology used in the proposed thesis for cost-effective 3D luminescence lifetime determination based on the combination of rolling digital shutter and light sheet illumination. The chapter proceeds to detail the optical setup essential for implementing the designed methodology. Then, it sequentially introduces the fabrication of the luminescence probe, the structure of the verification platform, and the software utilized in the experiments.

Chapter 4 provides a series of experiments that validate the effectiveness of the proposed rolling-shutter based luminescence lifetime measurement, as well as the detailed analysis of the signal captured. By assessing the readout signals from a steady-state probe and multiple probes with different oxygen tension, the design shows sub-millimeter spatial resolution and sub-microsecond temporal resolution with good stability.

Chapter 5 concludes the thesis with a brief discussion on the critical contribution made in the thesis and summarizes the results from the experiments. The advantages and the targeting applications of the oxygen sensing system proposed in this thesis are addressed. The limitations and the possible aspects for future improvement are also mentioned.

1.3 Contribution

Current methodologies for accurate 3D oxygen concentration measurement often require specialized equipment and expertise, posing challenges for fast prototyping and assessing oxygen levels in small tissue engineering or cell-related research projects. Building upon a previous proposed luminescence lifetime measurement technique using a rolling-shutter camera, this thesis introduces a cost-effective light-sheet imaging system that can conduct luminescence lifetime imaging for volumetric oxygen concentration measurement in 3D cell culture samples. A corresponding lifetime determination algorithm is included in the thesis, improving the temporal resolution to sub-microsecond level compared to previous work. Additionally, a MATLAB application has been developed to facilitate signal processing from images captured by the system. This thesis aims to serve as a comprehensive guide for the straightforward implementation of 3D oxygen sensing in related projects with limited budgets, while still achieving a high level of accuracy.

Chapter 2: Introduction

Accurate measurement of oxygen concentration using optical techniques in both 2D and 3D, spanning from the micro to macro scales, has seen significant advancements over recent decades. This chapter will provide an overview of the core principles underlying oxygen concentration measurement through phosphorescence lifetime monitoring, discuss traditional instruments utilized for precise imaging oxygen concentration imaging, and describe several investigations that to apply alternative optical methods other than those integrated with microscope platforms for specific applications. A core challenge lies in achieving a balance between the performance and cost of oxygen concentration measurement through optical techniques when compared with these established methods. Finally, the fundamentals of polymer-encapsulated phosphor probe typically used in phosphorescence lifetime imaging for oxygen concentration measurement will be introduced.

2.1 Optical Sensing of Oxygen Concentration

Among the various optical techniques to measure oxygen concentration, quantifying the oxygen's quenching effect on the luminescence emission is a common approach. A brief introduction to the theory and the implementation of the traditional measurement devices will be presented in section 2.1.

2.1.1 Photoluminescence

Photoluminescence is light emission from any substance after the absorption of photons. Following excitation, various relaxation processes typically occur in which other photons at lower frequencies are re-radiated. Depending on the nature of the excited state of the luminophore, time periods between absorption and emission can range from nanosecond-level for fluorescence to millisecond-regime for phosphorescence. According to the Jablonski diagram (shown in Figure 2.1), the electronic ground state of the luminophore is denoted by a singlet state S_0, and other higher discrete electronic states are depicted by S_1 and S_2. The transitions between states are denoted as vertical lines to indicate the instantaneous process of photon absorption (which occur in about 10^{-15}s). After the photon absorption, electrons at higher excited states (S_2 or above) will relax rapidly to S_1 through non-radiative process (internal conversion, IC) and later fall back to the ground state S_0 accompanied by photon emissions. These processes are often categorized as fluorescence and phosphorescence [32].

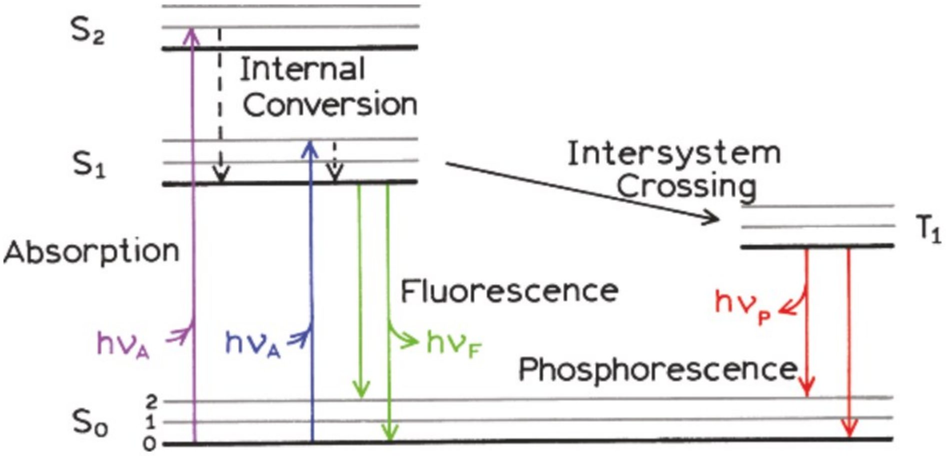

Figure 2.1 Jablonski diagram (Reproduced from [33]).

Fluorescence, where the emission is a result of the direct return from state S_1 to state S_0, is a fast process and typically in the time order of 10^{-9} - 10^{-4} s. Since a portion of the energy from the absorbed photon is dissipated, the reemitted photons will have lower energy than did the excitation photons, i.e., shift to longer wavelengths. For phosphorescence, the excited state electrons in the luminescent molecules can also undergo intersystem crossing (ISC) where they enter a state (triplet state T_1) with altered spin multiplicity (spin conversion). Transition from T_1 back to the singlet ground state S_0 is generally associated with a shift to even longer wavelengths compared to the emission in fluorescence. This process is quantum mechanically forbidden, causing the rate constant for triplet emission to be several orders of magnitude smaller than those for fluorescence. As a result, the time order of phosphorescence process is 10^{-4} to 10^{-2} s.

The lifetime of the excited luminophore in the absence of non-radiative energy dissipation through the interaction with the environment is given by [33]:

$$\tau = \frac{1}{\Gamma} \tag{2.1}$$

where Γ is the probability of the photoluminescence emission of a type of excited fluorophore and defined as the photon-emissive rate of the luminophore. In this case, the luminescence emission is simplified into an isotropic pattern, where all the directions with respect to the luminescent probe have the equal probability to observe the emitted photon, without any polarized effect. Under such conditions, the macroscopic emissive intensity decay from a mass population of the excited molecules after a short pulse light excitation can be described by the single-exponential curve given the emissive rate $\frac{1}{\tau}$ [33]:

$$I(t) = I_0 e^{-t/\tau} \tag{2.2}$$

where I_0 is the initial intensity after the excitation. It also indicates another definition of the lifetime as equal to the time point when the emissive intensity decreases to $1/_e$ of the initial value (see Figure 2.2). Single-exponential approximation can offer satisfactory precision for the oxygen concentration-related phosphorescence lifetime measurements which will be discussed in the following sections.

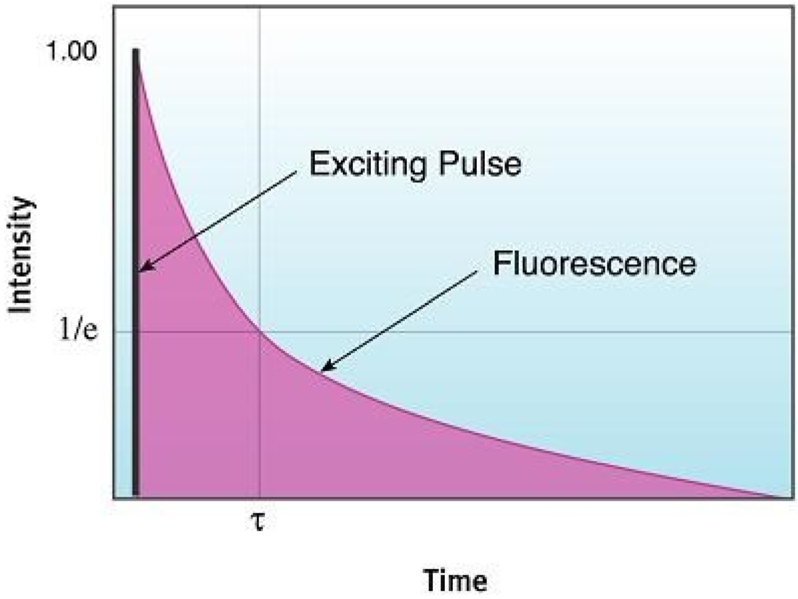

Figure 2.2 Luminescence (fluorescence) decay curve following an exciting pulse.

However, for comprehensive understanding of luminescent molecule characteristics and environmental interactions, anisotropy in the emission should be examined and multi-exponential analysis should be deployed [34]. It is universal that the light emitted by a luminophore has unequal intensities in different directions in response to the polarization state of the excitation light. Such anisotropy can wrap delicate environmental variables into the luminescent decay profile. Using multiple exponential analysis can better resolve the decay curve and reveal more detailed information.

2.1.2 Quenching of Photoluminescence

The absorbed energy from the excited-state luminophores can be transferred to other ground-state molecules in the surrounding environment. This portion of the energy is usually dissipated through other non-radiative processes and hence causes decrease in the photoluminescent emissions. Such decreases in the luminescence are called quenching. Quenching can occur by a variety of mechanisms, with collisional quenching being the predominant mode. In the case of collisional quenching, the excited-state luminophore is deactivated to the ground state upon a diffusive encounter with the quencher [33]. This mechanism is suitable for sensing oxygen concentration using optical methods, as oxygen is a typical quencher to a wide range of fluorescent and phosphorescent molecules and the extent of the decrease in the luminescence can be analyzed to determine the oxygen level around the luminescence dye. Since the molecules involved are not chemically altered in the process, the luminescent probe can be made inert and will not affect microenvironment in the 3D cell culture constructs, assessing the oxygen concentration by observing the luminescent emissions.

The study of oxygen as a luminescent quenching molecule has a long history [35]. The quenching effect caused by molecular oxygen, like many other quencher in collisional quenching, can be described by the Stern-Volmer equation [36]:

$$F_0/F = 1 + K_{SV} \cdot pO_2 \tag{2.3}$$

where F_0 and F are the luminescence intensities in the absence and presence of the quencher (molecular oxygen), K_{SV} is the Stern-Volmer quenching constant, and pO_2 is the on-site partial pressure of oxygen around the luminescent dye. Theoretically, by utilizing two end points ($F_0 - pO_2^{Depleted}$, $F_0 - pO_2^{Saturated}$), we can obtain the intensity – oxygen level curve from Eq. 2.3 for any luminescence intensity and its corresponding oxygen concentration. However, the measured luminescence intensity is highly correlated with the structure of the sample and the instrument design. Light absorption and scattering along the light path from inside the sample and through the optical system are impractical to accurately calculate. Consequently, quenching assessment based on intensity measurement requires calibration for each specific experiment configuration or deployment of a reference luminescent dye with no response to the quencher (ratiometric luminescent oxygen sensing [37-39]).

Meanwhile, unlike static luminescence intensity measurement, the single-pulse excitation response (shape of the emission decay curve) is a robust indication of the luminescence as the curvature is only correlated with the photon emissive rate (depicted in Fig. 2.2). The type of the luminophore and the quencher concentration will determine the rate of the radiative emission, which will not be changed by variation in the illumination, amount of the dye, sample structure, absorption and scattering along the optical path. As presented in 2.1.2, luminescence lifetime can be a straightforward indicator for the characteristics of the decay curve as long as the single-exponential fitting can provide a good approximation. The relationship between the lifetime and the quencher concentration (pO_2) can also be described by the Stern-Volmer equation obtained through simple derivation [33].

As the emissive rate is constant, the luminescence intensity observed for a luminophore is proportional to its excited-state concentration $[F^*]$. For continuous illumination, we will have a stabilized constant excited-state population in the absence of the quencher [33]:

$$\frac{d[F^*]}{dt} = E - (\Gamma + k_{nr})[F^*]_0 = 0 \qquad (2.4)$$

where E is the excitation power, Γ is the luminescent emissive rate, and k_{nr} is the non-radiative energy dissipation in the absence of the quencher. Similar to Eq. 2.1, we will have the luminescence lifetime in the absence of the quencher as [33]:

$$\tau_0 = (\Gamma + k_{nr})^{-1} = \gamma^{-1} \qquad (2.5)$$

In the presence of a quencher, the excited-state population when stabilized will be [33]:

$$\frac{d[F^*]}{dt} = E - \left(\gamma + k_q \cdot pO_2\right)[F^*] = 0 \qquad (2.6)$$

$$\tau = \left(\gamma + k_q \cdot pO_2\right)^{-1} \qquad (2.7)$$

From Eq. 2.4 and 2.6 we have [33]:

$$\frac{F}{F_0} = \frac{\gamma}{\gamma + k_q \cdot pO_2} = \frac{1}{1 + K_{SV} \cdot pO_2} = \frac{\tau}{\tau_0} \qquad (2.8)$$

which also coincides with the Stern-Volmer equation in Eq. 2.3. Change in both intensity and lifetime of the luminescence due to quenching can be used to measure the oxygen concentration. Lifetime measurement is evidently preferred as it is not affected by signal attenuations and distortions along various optical paths in the samples, while measuring intensity are usually conducted over cell culture microwells or microfluidic devices as the optical signal transmitting path can be fixed [21, 40].

2.1.3 Instruments for Luminescence Lifetime Measurement

Luminescence lifetime measurements require considerable expertise and specialized equipment to measure the rapid temporal dynamics of luminescent processes, where the timescales usually range from nanoseconds to microseconds. Typically, costly yet sensitive and highly precise imaging systems such as confocal and multiphoton laser scanning microscopes are employed to provide gold-standard results, exhibiting capabilities not only to resolve nanosecond-level fluorescence lifetime, but also to offer micrometer-scale [16, 17] or even intracellular-level spatial distribution of oxygen [18, 19]. Within these implementations, time-correlated single-photon counting (TCSPC) or time-gated single-photon counting (TGSPC) based on photomultiplier tubes (PMTs) or single-photon avalanche diodes (SPADs) are deployed as detectors.

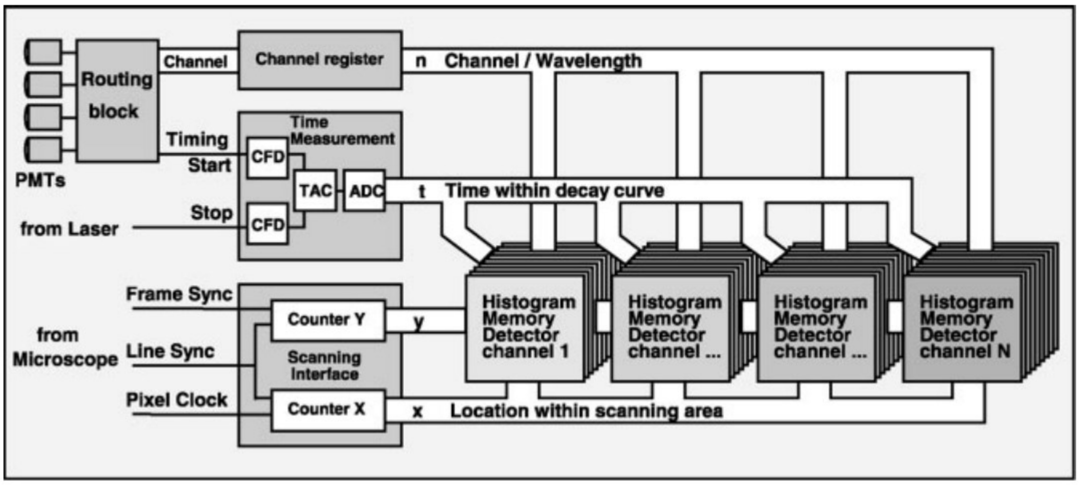

Figure 2.3 TCSPC electronics (Reproduced from [41]). The emitted photon arrival time correlated with the excitation laser pulse is recorded by the time-to-digital converter (TDC). The x, y positions are recorded synchronously by the scanning system.

Figure 2.3 shows the diagram of TCSPC system based on multiple PMTs [41]. When a photon is detected by any one of the PMTs, the system will determine the photon arrival time within the luminescence decay curve and the corresponding location of the signal within the scanning area. After numerous excitation - arrival recording cycles, a histogram of photon arrival event counts can be drawn, which corresponds to the shape of the decay curve because more event counts over a time stamp indicates larger probability of emission or intensity when observing a mass population of excited radiative dye molecules.

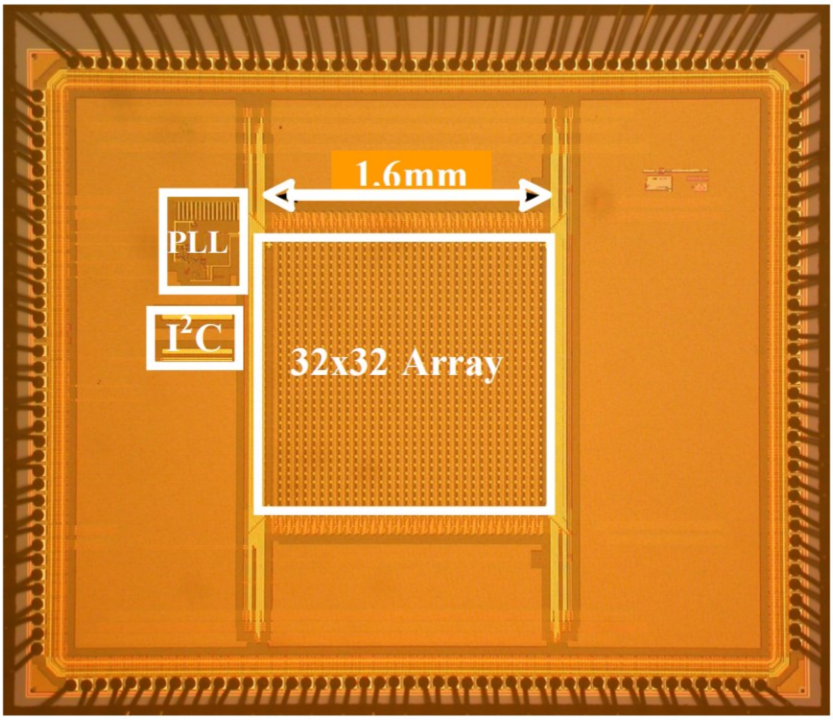

Figure 2.4 Photomicrograph of a 32x32 SPAD pixel array (Reproduced from [42]).

Advances in SPAD design facilitated the fully solid-state single-photon detector array with on-chip integrated TDCs as shown in Figure 2.4. In such chips, the pixel-array is also read-out with the address-event approach as the traditional system does [43]. However, for a large array size designed for high-resolution imaging, the time stamp information for each detected photon arrival event leads to high throughput data transmission requirements, together with the heavy load of external processing to extract the lifetime information. As such, an alternative approach that is called time-gated single-photon counting (TGSPC) is also favored, shown in Figure 2.5. In this method, the number of detected photon events within two or more time-windows after the pulsed excitation is recorded to extract the lifetime, dramatically reducing the streaming data volume.

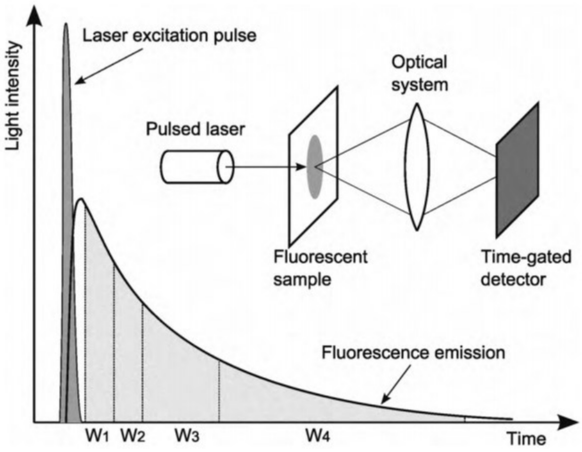

Figure 2.5 Time-gated luminescence lifetime measurement principle

(Reproduced from [43]).

All of the above technologies offer fast operating speed capable of resolving nanosecond-level lifetime with extremely high costs. Even for phosphorescence which has a slower decaying rate and wider dynamic range with respect to the quenching effect, the lifetime in the timescale of microsecond still needs to be resolved by megahertz-level sampling rate of the image detectors that are rarely available from budget-friendly off-the-shelf options.

2.2 Oxygen Measurement in Cell Culture Applications

Except for the advanced imaging systems combining high-speed single-photon detectors, numerous research designs have been proposed recently to provide solutions to application-orientated oxygen sensing tasks based on luminescence lifetime in cell culture samples. In these cases, the customized setups can reduce unnecessary costs by using specific components according to the samples and eliminating some redundancy in general purpose systems, such as scanning systems, high resolution imagers, and advanced microscope optics. However, the drawback of high cost to measure luminescence lifetime can hardly avoided owing to the requirements in spatial and temporal accuracy.

2.2.1 Single-Point Measurement

Single-point oxygen sensing is sometimes favored in projects that need fast oxygen level measurement without the requirement to assess the spatial distribution of oxygen within the volume of the samples. A single solid-state detector and the corresponding illumination can be adjusted to optimize the luminescence excitation and emission detection over the probe at the fixed position within the sample [22, 23].

A typical single point oxygen probing configuration in cell culture is shown in Figure 2.6. Epithelial cells are cultured in hydrogel matrix and a 0.5 mm thick phosphorescence dye-embedded polymer film is deployed at the bottom. Light from LED excites the sensor and the corresponding emission can be detected by the silicone photomultiplier. The structure only requires minimized optical tuning and the oxygen concentration at the site with lowest oxygen supply rate (bottom layer) can be obtained rapidly.

Figure 2.6 Schematic of oxygen sensing via a single probe inside hydrogel containing cells (Reproduced from [44]).

There is also single point measurement based on professional TCSPC system in living animal imaging experiments due to a variety of constraints in coupling optics and animal organs, see Figure 2.7.

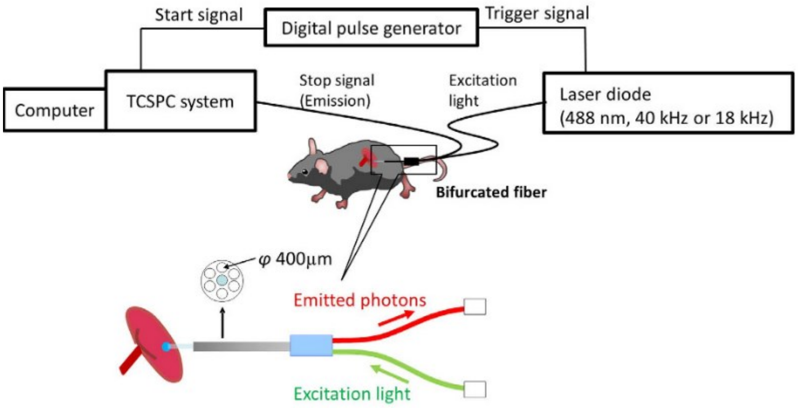

Figure 2.7 Schematic diagram of the phosphorescence lifetime imaging system for living mouse. The excitation light and the emission light are guided to and collected from the kidney by an optical fiber, respectively (Reproduced from [24]).

2.2.2 Oxygen Distribution Measurement

Spatially resolved oxygen distribution is a vital measurement parameter in 3D cell culture matrix to study cell metabolism with respect to external/internal factors, or enable the assessment of the oxygen supplying conditions for the success of *in-vitro* tissue growth in tissue engineering applications. Apart from the instruments with high-end single-photon detectors integrated in confocal/multiphoton microscopes, there are numerous off-the-shelf sCMOS cameras especially designed to conduct lifetime measurement tasks. Although the prices of these scientific cameras are still high, the compact lifetime measurement systems enable fast construction of an oxygen mapping setup for various sample geometries without the large workload in optical designs.

In [25, 45], the authors applied a commercially available scientific cameras that are capable of far-field determination of luminescence lifetime, as shown in Figure 2.8 and 2.9. In [25], they utilized a Tpx3Cam optical camera to directly image the varying oxygen concentration caused by the oxygen uptake by the respiring cells precipitated at the bottom of the tube.

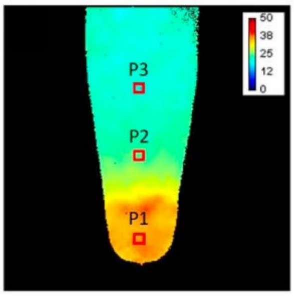

Figure 2.8 Lifetime gradient caused by varying oxygen concentration in a tube with respiring live cell precipitated in the bottom. Phosphorescence dye probes are dispersed in the culture medium and the image is taken at the side view (Reproduced from [25]).

In [45], a FLIM (fluorescence lifetime imaging microscopy) camera is applied, where the observation of the lifetime correlated with the oxygen distribution in the rhizosphere of the aquatic plant can be achieved at meter-long distance (see Figure 2.9).

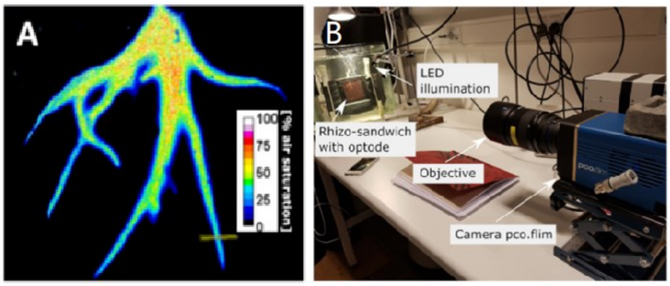

Figure 2.9 (A) Phosphorescence lifetime mapping in the rhizosphere of the aquatic plant. (B) Demonstration of the FLIM camera imaging experiment of long distance observation. (Reproduced from [45].)

Not only the fast luminescence lifetime imaging prototyping can be achieved by the cameras introduced above, but those cameras can be also integrated in advanced optical systems and conduct high-resolution microscopic imaging with minimal effort in configuring lifetime extraction or other image data processing. The primary drawback of such solutions remains the high cost, attributed to their limited market demand and constrained production capacity. This renders them inaccessible to biological research groups in need of oxygen distribution measurement but lacking sufficient funds.

2.2.3 Wide-Field Lifetime Measurement Using Economic Imager

Even though the majority of the photoluminescence lifetime measurement systems consist of professional detectors with high sensitivity and sampling rate and are capable of conducting time-correlated single-photon counting (TCSPC) or time-gated single-photon counting (TGSPC) tasks, there are also numerous attempts to utilize commercially available and economic CMOS or CCD imagers to achieve wide-field lifetime measurements.

Theoretically, fast frame rate cameras that achieve 10 kHz-level can perform TCSPC at microsecond resolution. By synchronizing the camera and the excitation source, where the camera will collect a defined number of frames after each excitation pulse, arrival-time histogram of single-photon events at each pixel on the camera's sensor array can be extracted from the sequence of consecutive frames [46], as shown in Figure 2.10.

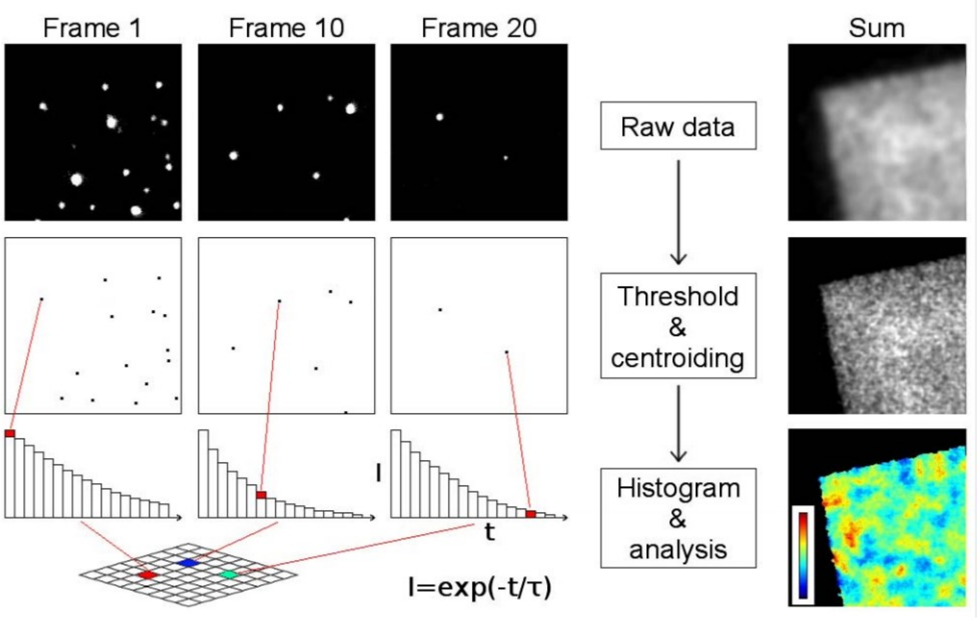

Figure 2.10 Schematic of TCSPC using an image sensor. Histograms of photon arrival times are established over each individual pixel from a sequence of consecutive frames (Reproduced from [46]).

However, sensitivity of such imagers is usually too low for single-photon detection. The image intensifier, which converts single-photon event to magnified current and then converts the current back to light signals, is required to integrated in front of the CCD or CMOS cameras (See Figure 2.11). A photoelectron, which is created by an incoming photon hitting the photocathode of the image intensifier, is accelerated into a microchannel plate (MCP) by a high voltage and creates more electrons by its impact when travelling along the channels of the MCP. The resulting massive current flow will convert back to photons when reaching the phosphor plate and create a prominent phosphorescence emission process as an indication of the initial single-photon event. The transit time from the single-photon arrival to the phosphorescence is short enough to preserve the photon arrival time with respect to the timescale of the TCSPC task to measure microsecond-level photoluminescence decay.

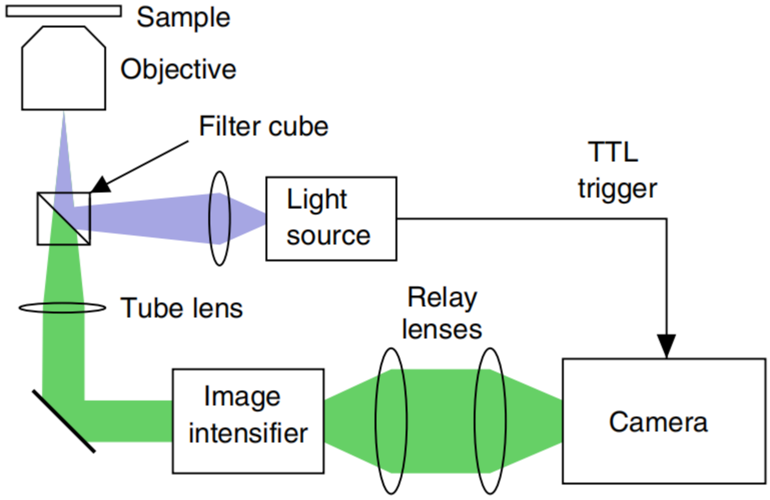

Figure 2.11 Schematic of TCSPC system based on conventional CCD/CMOS camera. An image intensifier is coupled with the image sensor to enable single-photon event detection (Reproduced from [46]).

In this configuration, the time resolution is limited by the exposure time of each frame whose minimal value can hardly be below 10 μs. As such, uncertainties in the arrival time of each single-photon event are introduced. To improve the accuracy and proceed the temporal resolution into sub-microsecond level, phosphor’s afterglow at the end stage in the image intensifier can be utilized to estimate the arrival time with sub-camera exposure time precision, instead of directly using the frame capture time [47-49] (see Figure 2.12).

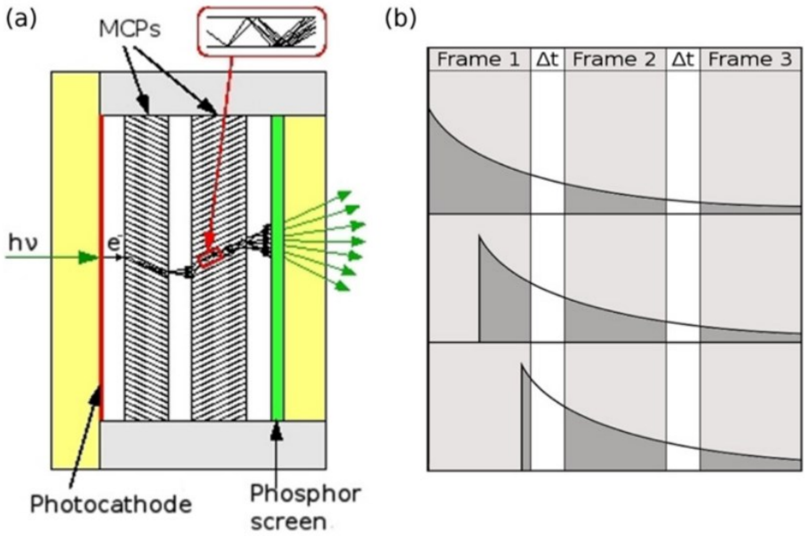

Figure 2.12 (Reproduced from [31].) (a) Schematic of an image intensifier that converts a single-photon event to a short pulse-induced phosphorescence emission. (b) Demonstration of sub-camera exposure period resolution of photon arrival time measurement. The integration values from consecutive frames can be utilized to approximate the photon arrival time within the exposure duration of the first frame encountering the phosphorescence emission.

Instead of using the time stamps of individual frames, which have spacings of several tens of microsecond, to refer to the photon arrival time, the pixel integration results from successive frames can be analyzed to determine the time point of the single-photon event within the exposure duration of one single frame. As the afterglow of the phosphor screen decay is also a phosphorescence emission process, variations in the phosphor decay function are small when observing the brightness of the amplified single-photon events. The ratio of the pixel values between the first and the second frames right after a single-photon event will decrease for the photon arriving later during the exposure time of the first frame, as depicted in Figure 2.12 (b). As a result, sub-microsecond temporal resolution can be achieved, guaranteeing a promising potential to be utilized in a variety of oxygen-sensitive phosphorescent dyes.

Yet the expense of the image intensifier, together with a high frame rate camera, is still a large amount and inaccessible in most of the bioengineering and tissue engineering labs, hindering the practice in real applications. Using cost-effective and conventional instruments to achieve accurate oxygen sensing is still favored in the related fields.

2.3 Oxygen-Sensitive Phosphorescent Probe

While the mechanisms and modelling of the phosphorescence quenching by the oxygen molecule have been investigated thoroughly, few materials have ever explained the physics during the oxygen sensing process of phosphorescent probes in a brief and clear manner. Two important requirements must be considered to translate phosphorescence quenching theories into biomedical oxygen measurement applications:

1) Instead of directly dispensing the free-form phosphorescent molecules in the aqueous environment to be tested, polymer materials should be utilized to encapsulate the dye.
2) The absolute dissolved oxygen concentration in aqueous environment can be around 40 times lower than the oxygen concentration in gaseous form in air (1 atm). The oxygen molarity in air is 35.67 mol/L, where in air-equilibrated water the oxygen concentration becomes 0.225 mol/L at 37 °C. The phosphorescent polymer-encapsulated probes should be properly fabricated to exhibit good dynamic ranges and optical responses over the changes of dissolved oxygen levels in aqueous

environments such as cell culture setups. And their performance should closely match the gaseous case where the oxygen concentration has more significant variations.

This section will discuss the points raised above and give a straightforward view on oxygen sensitive probe based on phosphorescence oxygen-quenching effect.

2.3.1 Polymer-Encapsulation of Phosphorescent Dye

There are several reasons to deploy dye in an encapsulated form:

First of all, isolating the dye molecules from direct contact with the aqueous environment can mitigate undesirable interactions between the dye and its surroundings, thereby avoiding disruptions in luminescence emission. The photophysical character of an excited dye molecule can be greatly affected by polar solvent molecules such as water or alcohols [50]. Intramolecular charge transfer (ICT) can be caused by the intermolecular hydrogen bonding of the protic solvent water to the excited-state dye molecule. Consequently, part of the energy in the excited-state dye molecules will be dissipated through radiationless deactivation, in addition to the quenching effect owing to oxygen, upon the luminescence emission. Similarly, cross-sensitivity of the luminescence probe to other parameters in the environment should be considered. The luminescence of an indicator can also be affected by the presence of ionic species, which are common components in the cell culture media [51]. Ionic species and water will be of less relevance if the dye molecules are incorporated in polymers which can act as permeation-selective membrane for those factors.

On the other hand, cytotoxicity introduced by the dye molecule should be the main concern for the success of cell/tissue growth [51]. Encapsulation of the dye into a polymetric matrix and isolating it from the cells can greatly reduce the toxicity, although the phototoxicity caused by the production of singlet oxygen during the emission process cannot be eliminated completely.

To achieve the immobilization of luminophores, the host polymer should be compatible and inert to luminophores, provide long-term stability, and have appropriate oxygen permeability [52]. Polystyrene (PS) is thus widely used as host polymer to encapsulate oxygen sensitive luminophores owing to its inertia and biocompatibility [53, 54].

2.3.2 Oxygen Diffusion and Probe Response

Preventing cross-talk between the dye and matters other than oxygen is only part of the consideration to use polymer encapsulation to separate the dye and the culture environment, as the previous subsection explained. To proceed with the discussion and examine the second requirement, the dynamics of oxygen sensing when using phosphorescence probes should be introduced first.

The diffusion of gas is along the chemical potential gradient [55, 56], where in most discussions it is substituted by the concentration gradient. However, diffusion may not always be from the high concentration to low concentration, especially for the gas diffusion at gas-liquid and liquid-solid interfaces. In a system at equilibrium state, the chemical potential of a component inside should be consistent across the whole system. Suppose we are examining the polymer-encapsulated phosphor probes (see Figure 2.13):

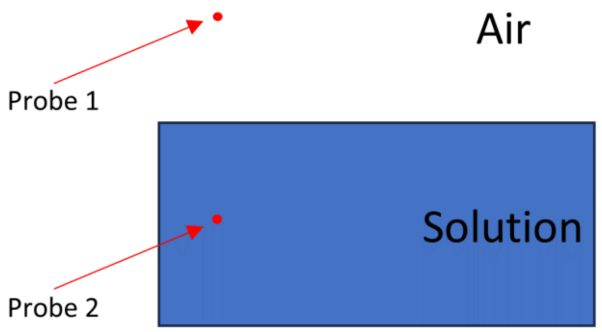

Figure 2.13 Two identical polymer-encapsulated phosphor probes are placed in a equilibrated system consisting of air and aqueous solution. One probe is placed in the air while the other is immersed in the solution.

For the oxygen concentrations inside two probes, they should be consistent as well, as the chemical potentials of the oxygen molecule are the same inside the whole system after fully equilibrium. Consequently, the oxygen level in solution or even solid can be expressed as a percentage or partial pressure equivalent to the oxygen fraction in the gaseous phase in the system/surrounding environment. Hence, the polymer probe can exhibit the same dynamic range in response to the corresponding oxygen partial pressure changes, whether it is in the solution or exposed to open air.

The polymer material should be chosen carefully to obtain a reasonable oxygen concentration range in the probe in response to the variations in the oxygen level during the measurement [57]. As the excessively high oxygen permeability will lead to a narrow linear dynamic range [58], polystyrene is also qualified with an appropriate permeability resulting in single exponential calibration curve with a single quenching constant [59, 60]. This is to guarantee a good dynamic range of the measurement, where the quenching effect should vary significantly between the hypoxic and the normoxic conditions. The polymer-dye ratio should also be considered to prevent the formation of the dye aggregates and the resulting concentration quenching [61].

2.4 Summary

This chapter firstly discussed principles of oxygen concentration measurement based on photoluminescence quenching effect, revealing the advantages of measuring lifetime rather than intensity, as well as the difficulties in reaching the temporal resolution requirement for precise lifetime measurements. Then we introduced a series of traditional and innovative methods to conduct lifetime measurements, exposing the fact that there is still lacking a balanced solution with moderate cost while achieving satisfactory spatial and temporal resolution to measure oxygen distribution in cell culture and tissue engineering applications. Thirdly, we briefly explained the reason why polymer-encapsulated phosphor probe, especially when the host material is polystyrene, can serve equivalently well in both gaseous and aqueous environments, which is part of the fundamental of oxygen-sensitive optical probe in the oxygen sensing industry [53, 54, 59, 60]. Despite that the oxygen sensing luminescence probes have been deployed in various scenarios, the precise determination of the luminescent signals always requires expensive instruments and expertise [16, 19, 20]. Hence, there exists ample room for innovation and creativity that can contribute to the advancement of 3D oxygen imaging and oxygen distribution mapping techniques leveraging cost-efficient solutions while maintaining qualified accuracy in the cell culture research. This thesis is driven by this realization and aims to offer a design that enhances the capabilities of the biomedical research community.

Chapter 3: Experimental Setup and Methods

In this chapter, a cost-effective phosphorescence lifetime imaging design for measuring the lifetime of oxygen-quenched phosphorescence emission with both impressive temporal and spatial resolutions in three dimensions will be presented, alleviating the trade-off between cost and performance in traditional imaging modalities. The primary method for measuring phosphorescence lifetime using a rolling shutter mode CMOS sensor will be introduced. Subsequently, the optical setup and experimental designs to validate the effectiveness and capability of this method will be presented.

3.1 Phosphorescence Lifetime Measurement Using Rolling Shutter CMOS Sensor

The cost-effective lifetime measuring approach proposed in this work leverages the use of the rolling-shutter effect in consumer-level CMOS cameras to perform high-fidelity frequency-domain lifetime measurement through data processing.

Even though the phosphorescent dyes, whose lifetimes usually lies in the span of microsecond, are actively utilized in oxygen sensing, measurement of the exponential decay in phosphorescence intensity (time-domain) still requires high sensitivity and megahertz-level sampling rate to resolve the decaying curve. This process can only be achieved with expensive devices like silicon photomultiplier or avalanche photodiode rather than a commercial image sensor [44]. An alternative way is to utilize the rapid lifetime determination algorithm which only requires a limited number of images to determine the parameters of a single decaying process but needs low-level hardware control to ensure high synchronization between the image sensor capturing and the excitation signal [62].

To enable the economic but "slow" camera in phosphorescence lifetime determination, frequency-domain method shall be leveraged. Unlike the time-domain method introduced in 2.1.3 and 2.2.3, which uses a single short pulse for excitation, the frequency-domain method utilizes continuous but sinusoidally amplitude-modulated excitation. This results in the continuous emission from the phosphors which follows the modulation frequency of the excitation while exhibiting a phase difference due to the decaying nature of the excited states of the phosphor molecules.

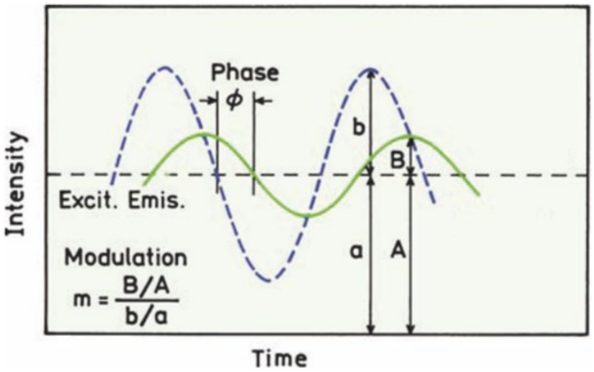

Figure 3.1 (Reproduced from [63].) Schematic of the fluorescent response to the sinusoidally amplitude-modulated excitation light. The delay in phase can be seen as the frequency-domain counterpart of the fluorescence emission lifetime in response to a single pulse excitation.

Suppose the sinusoidally modulated excitation light is:

$$L(t) = a + b \sin \omega t \tag{3.1}$$

As the emission forced to respond with the same frequency, one can assume that the excited-state fluorophore population is:

$$N(t) = A + B\sin(\omega t - \varphi) \tag{3.2}$$

As Eq. 2.2 shows, the intensity decay of the fluorescent emission is a single exponential, while the time-dependent differential equation of the excited-state population can be written as [33]:

$$\frac{dI(t)}{t} = -\frac{1}{\tau}I(t) + L(t) \tag{3.3}$$

Since the intensity of the emission can be assumed to be proportional to the excited-state population, Eq. 3.3 can be reformed by substituting Eq. 3.2 into it [33]:

$$\omega B\cos(\omega t - \varphi) = -\frac{1}{\tau}[A + B\sin(\omega t - \varphi)] + a + b\sin\omega t \tag{3.4}$$

By equating the constant terms and terms in $\sin\omega t$ and $\cos\omega t$, one can have the relationships between those coefficients, where most importantly the equation, which directly links the time-domain fluorescence emission lifetime to the phase shift in the emission compared to the modulation of the excitation, can be found [33]:

$$\tan\varphi = \omega\tau \tag{3.5}$$

According to Nyquist sampling theorem, the measurement of this phase difference can be conducted at a considerably low sampling frequency in kilo-Hertz level, while resolving the decay of the phosphorescence emission in response to a short excitation pulse in time-domain measurement requires at least mega-Hertz level sampling speed for lifetime in micro-seconds.

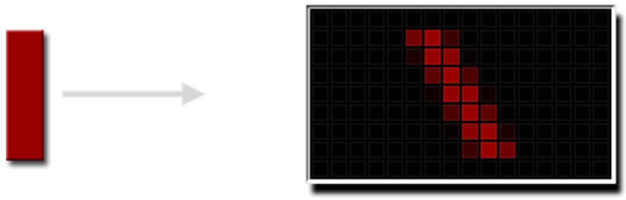

Figure 3.2 The rolling shutter effect in photography when filming a fast-moving object. The image position of the object is tilted as the shutter sweeps across the pixel array downward, which makes the start time of the exposure of each line of pixels lag a certain time increment than the previous line.

To restore the phase shift, the rolling shutter effect is leveraged as a fast-sampling mechanism. Pixels on the rolling mode CMOS sensor are sequentially activated in rows rather than all at once, as in global shutter mode. The rolling shutter effect happens when the object's moving speed is relative fast to sensor speed and is usually regarded as an unpleasant distortion in conventional photography (See Figure 3.2). However, the compact peripheral circuit design in a rolling shutter CMOS helps it excel its global shutter competitor in terms of sensitivity and cost, as the driving circuitry can be shared by a group of pixels in rolling shutter mode and leaves more space for light-sensing components. As such, new and better rolling shutter sensors are still being developed and a series of computer vision research topics were once being actively conducted for the automatic removal of the rolling shutter effect [64-67]. On the other hand, the rapid row-scanning speed, exceeding 100k rows per second even in commercially available and economic camera modules, also enables rolling shutter's potential to sample periodic light signals at frequencies much higher than the conventional camera frame rate of 60 fps. This capability makes it possible to measure luminescence lifetimes at microsecond level by analyzing the fringes shown in the image that arise from the coupling of the image sensor’s digital shutter line-scanning and the intensity-modulated excitation light, as this method was firstly proposed in [68].

Since the temporal behavior of all the pixels in the same row on the CMOS sensor are consistent, the position of the image of the luminescent probe can be tuned to cover the same range of pixel rows as the excitation light spot locates (See Figure 3.3 (a)). As the shutter sweeps along the pixel rows, the temporal variations in both the excitation light and the emission light can be recorded simultaneously through the pixel integration processes, maintaining their phase difference. When both the excitation and emission signals vary periodically at the same frequency, the resulting fringe patterns will be observed as shown in Figure 3.3 (b). As depicted in Figure 3.3 (c), the least square curve regression algorithm was applied to the readout sequences of the fringe patterns to extract the phase shift between the excitation and the emission signals.

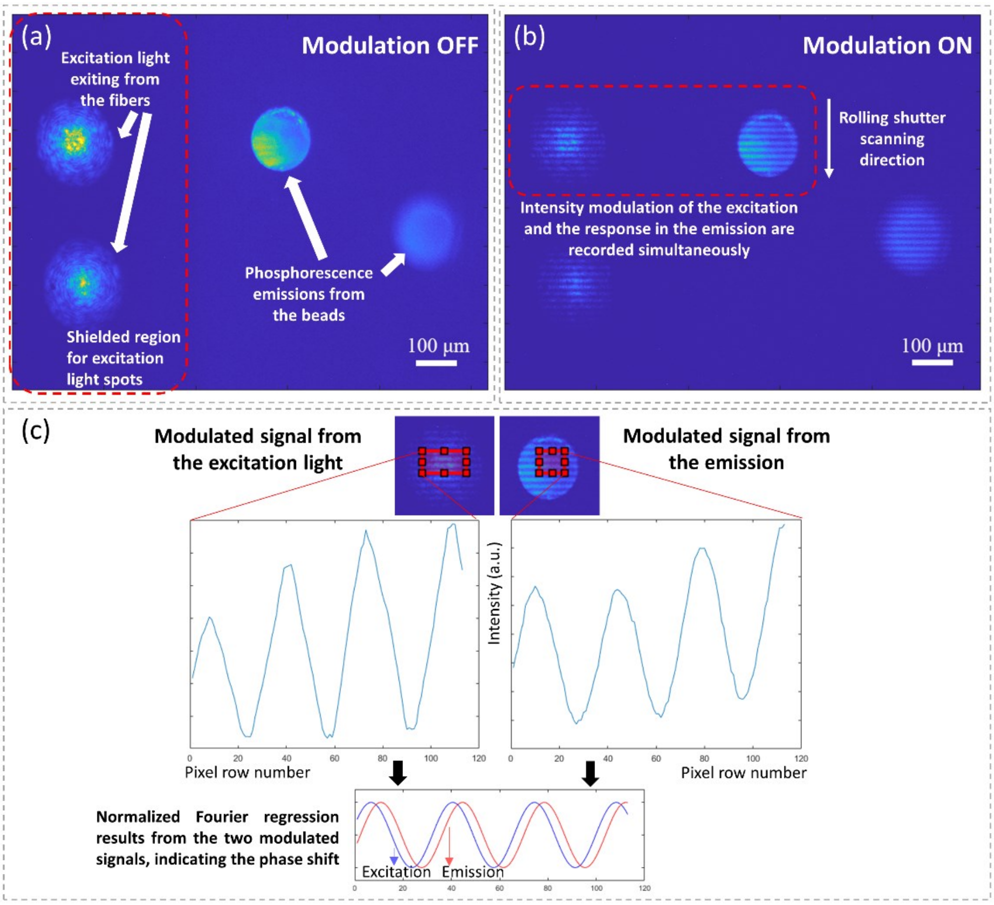

Figure 3.3 (a) Reference excitation light spots (in dashed line square) and the corresponding images of the phosphorescent probe. (b) Fringe patterns on the images of the excitation light and the emission light when the excitation light is under intensity modulation. (c) Phase difference extraction from the two signals in (b) by leveraging the least square curve regression algorithm.

The corresponding intensity waveforms in Figure 3.3 (c) are obtained by plotting the readout values along the row number. Based on the 4 kHz modulation and 7 us/line shutter scanning speed, 100 – 120 rows are included in the regions of interest (ROIs) that can at least cover 3 modulation cycles for accurate phase extraction in the curve regression process. Meanwhile, the readouts on the same row were summed up to increase the signal-to-noise ratio, corresponding to 90 – 120 pixels in ROI widths which also depended on the light spot sizes. The lifetime of the phosphorescence emission can be calculated using Eq. (3.5) once the phase shift is obtained. The exposure time requires careful consideration to conduct a low-pass filtering effect by the integrate process and accommodate for the square wave TTL intensity modulation instead of sinusoids, as it will be explained in section 3.5 when discussing image acquisition.

3.2 Materials

To construct the optical system, a laser diode module (Laserland, 405nm, 200mW) serves as the excitation light source and is controlled by a driver (12V/2A DC, 200mW – 2W) that receives square wave TTL modulation signal (4kHz, 50% duty cycle) from a function generator (Tektronix, AFG 3022B). A 3:7 beam splitter (Thorlabs, EBP1), a multimode optical fiber (Corning), and a 3.5X beam expanding plano-convex lens pair (Thorlabs, LA1131-A f = 50mm, LA1229-A f = 175mm), a cylindrical lens (Thorlabs, LJ1695RM-A f = 50mm), and an objective (Carl Zeiss, 10X 0.22 NA) are utilized to generate the light-sheet and reference signal. The detection arm uses an imaging objective (Olympus, 10X Plan C Achromatic Dry Objective, infinity-corrected, 0.25 NA) and an emission filter (Semrock, FF01-593, 593nm long-pass) to collect luminescence signals, which are further captured by a CMOS camera (Alvium 1800U 501m NIR, image sensor: ON Semi AR0522).

Platinum(II)-5,10,15,20-tetrakis-(2,3,4,5,6-pentafluorphenyl)-porphyrin (PtTFPP, Frontier Scientific) serves as the oxygen-sensitive phosphorescence dye. Polystyrene polystyrene (PS, Sigma-Aldrich, average M_w ~280,000 by GPC) is utilized to encapsulate the dye. During the luminescent probe fabrication process, 5%wt polyvinyl alcohol (Sigma-Aldrich, M_w 13,000-23,000, 87-89% hydrolyzed) in water and dichloromethane (Sigma-Aldrich, anhydrous, ≥ 99.8%) are used to conduct flow focusing polymer bead generation.

3.3 Optical System

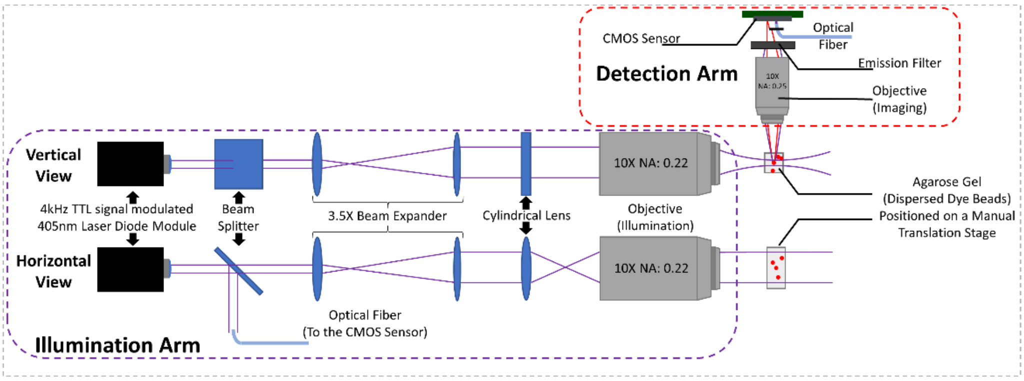

Figure 3.4 Schematic of the optical system. The low power microscope structure (Detection Arm) incorporates both light-sheet illumination (Illumination Arm) and a rolling shutter CMOS image sensor. Vertical and horizontal views of the illumination arm are provided respectively. The cubic sample can be positioned and swept through the illumination plane by utilizing a manual translational stage. To enable simultaneous capture of both excitation and emission signals, a portion of the excitation light is split at the source and directed to the CMOS sensor in the detection arm via optical fibers.

As depicted in Figure 3.4, the optical system is designed to facilitate rapid verification of the proposed low-cost luminescence lifetime determination method integrated on a low power microscope structure equipped with optical sectioning illumination, specifically a light sheet, to conduct 3D examination of the phosphorescent signals from the phosphor probes dispersed inside the cubic-shaped hydrogel samples.

The system comprises two main components: an illumination sub-system (illumination arm) that provides excitation to the phosphorescent probes deployed in the sample and a detection sub-system (detection arm) that collects the emission signals from the probes through the volume of the sample. The configuration of the illumination arm is adapted from an open-source integrated microscopy platform that provides recommendations for selecting user-friendly optical components for constructing a light-sheet setup [69]. The light sheet exhibits inherent optical-sectioning capability, as it illuminates the sample with a planar sheet of light that is comparable in thickness to the depth of field of the detection system [70]. Consequently, this technique can enhance the image contrast by minimizing out-of-focus background noise and reduce phototoxicity to the sample due to the highly confined light exposure.

The illumination arm, as shown in Figure 3.4 with both horizontal and vertical views, the excitation light originates from a laser diode module (Laserland, 405nm, 200mW) and is controlled by a driver (12V/2A DC, 200mW – 2W) that receives square wave TTL modulation signal (4kHz, 50% duty cycle) from a function generator (Tektronix, AFG 3022B). By adjusting the driving current, the maximum laser output power has been restricted to 100mW for all the experiments in this work. The output of the laser diode is a diverging elliptical beam circularized by the integrated aspheric lens in the module, resulting in a collimated beam with a 1.5 mm diameter. The light passes through a 3:7 beam splitter (Thorlabs, EBP1) before forming the light sheet. The reflected portion (30%) of the light is free space coupled to a multimode optical fiber (Corning) and directed to the CMOS sensor as the reference beam. Given that the output intensity of the fiber is significantly larger than the emission signal, concerns about coupling efficiency are negligible. Moreover, additional attenuation of the reference light through a neutral density filter is necessary to ensure the comparability of reference intensity and emission intensity. The transmitted portion (70%) forms the light sheet after passing through a 3.5X beam expanding plano-convex lens pair (Thorlabs, LA1131-A f = 50mm, LA1229-A f = 175mm), a cylindrical lens (Thorlabs, LJ1695RM-A f = 50mm), and an objective (Carl Zeiss, 10X 0.22 NA). This straightforward structure offers an approachable light-sheet illumination with a 20 um beam waist for performing sub-millimeter optical sectioning on cubic-shaped hydrogel culture constructs. Given that phosphor beads are dispersed within the samples and the optical setup is specifically utilized to examine the phosphorescence emission from individual probes, the light sheet's characteristics do not need to meet the same stringent requirements as those in 3D structural reconstruction applications.

The detection arm in Figure 3.4 is positioned orthogonally to the plane of the light sheet. An imaging objective (Olympus, 10X Plan C Achromatic Dry Objective, infinity-corrected, 0.25 NA) collects the phosphorescence emission from the phosphor probes excited by the light-sheet illumination in the agarose gel sample. After passing through an emission filter (Semrock, FF01-593, 593nm long-pass), images of the phosphorescence light form on the CMOS sensor, while approximately 25% of the sensor area is reserved for recording the excitation light spots by attaching a 3d-printed socket that holds the output end of the optical fibers towards the sensor. The overlap between the excitation and emission signals is avoided since the fiber socket shields the sensor area where the excitation spots lie. Therefore, light spots from the excitation signal directed by the optical fibers and the phosphorescence emission from the phosphor probe can be captured by the CMOS sensor at the same time. This simultaneous capture of two signals enables the frequency-domain luminescence lifetime measurement leveraging the rolling shutter scanning effect, which will be discussed in the following subsections. The positions of both the sample and the imaging arm can be tuned using manual translational stages, enabling adjustments of the illumination plane and the focal plane of the imaging objective for examining different depths of the hydrogel sample.

The infinity-corrected objective adopted in the detection arm is designed to ensure that all light rays originating from a single point on the specimen, at the objective’s working distance, exit the objective in a parallel way. In the standardized configuration, this objective requires the coupling with a tube lens to converge the light rays and form an image [71]. However, the cost of a tube lens could be comparable to the total cost of the other components. Alternatively, the infinity-corrected objective can still produce images without a tube lens by adjusting the specimen’s position further away from the focal plane (working distance), following the lens equation. This adjustment introduces enhanced spherical aberration, which we find tolerable as our focus is not on capturing the structural details of the sample. Instead, we are examining the rolling shutter scanning fringes across considerably large areas on the sensor. As a result, the detection arm features a simplified microscope structure.

3.4 Phosphor-embedded Microbead Preparation

The determination of phosphorescence lifetime from probes throughout the culture construct’s volume is the key process of 3D oxygen monitoring in this work. A phosphorescence dye (Platinum(II)-5,10,15,20-tetrakis-(2,3,4,5,6-pentafluorphenyl)-porphyrin, PtTFPP) that has a lifetime ranging from 21 µs to 70 µs [61], corresponding to air-equilibrated (20.9% of 1 atm pO_2) and oxygen-depleted (0% of 1 atm pO_2) conditions, respectively.

Spherical-shaped phosphor-embedded luminescent polymer beads were designed so that they can be conveniently integrated into customized cell culture constructs throughout its volume to enable spatial mapping of the oxygen concentration. The beads were fabricated using a co-flow glass capillary fluidic device [72]. In the 3D flow focusing device as shown in Figure 3.5 (a), the dispersed phase jet, which consists of 1 wt% polycaprolactone (PCL) and 0.0017 wt% PtTFPP in dichloromethane (DCM), is completely surrounded by the continuous phase flow irrespective of the hydrodynamic conditions of the wall, due to circular orifice geometry. The continuous phase is 5 wt% aqueous solution of polyvinyl alcohol (PVA, $M_w = 13{,}000 - 23{,}000\ g\ mol^{-1}$, 87-89% hydrolysed, Sigma-Aldrich), and it works as the emulsifying agent to stabilize the polymer/dye solution droplets in the flowing channel. The continuous phase solution can shear the dispersed phase into a sequence of droplets in the flowing channel, while the flow speeds of both phases can be controlled for the generation of different diameters of the droplets.

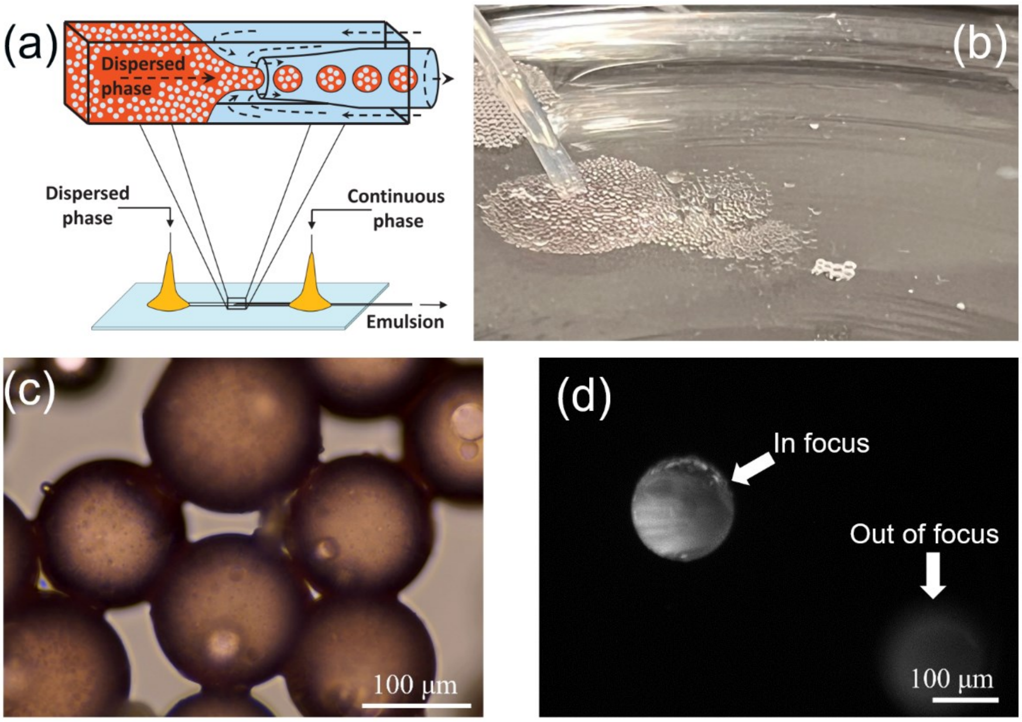

Figure 3.5 (a) Schematic diagram of the experimental setup with a magnified view of emulsion formation in the collection capillary of the microfluidic device [72]. (b) Oil-phase with dissolved polystyrene (PS) and PtTFPP dye droplets in the emulsion. After maintained in vacuum for an hour, the plastic beads will form. (c) 40X microscopic image of dye-embedded PS beads. (d) Image of the phosphorescence emissions from the PS beads captured by the optical setup shown in Figure 3.4.

The setup utilized glass capillaries with 1.3mm/0.5mm inner diameters as the flow channels, with the input ports of two solutions being syringe needles sealed by silicone rubber (Smooth-On, Dragon Skin 10). To obtain beads with diameters of 130μm, 2 mL/hr injection rate of the dispersed phase and 10 mL/hr injection rate of the continuous phase were applied. The microscopic images of the beads and their monochromatic luminescence image can be seen in Figure 3.5 (c) and Figure 3.5 (d), respectively. The uniform-size beads allow the embedded phosphors to exhibit a consistent response to the oxygen concentration changes in terms of the luminescence lifetime, excelling other geometries of probes.

3.5 Microfluidic Hydrogel Platform

To assess the system's spatial resolution and temporal precision in the context of 3D live cell constructs, a fluidic device that can generate varying millimeter-scale artificial oxygen gradients in agarose hydrogel samples was developed. Figure. 3.6 (a) shows the 3D model of this device. A 1 cm^3 well is built above a metal-mesh-embedded thin gas-permeable PDMS film, which supports the well over a hollow channel for nitrogen flow. A 2 mm-thick layer of 1% agarose hydrogel, mimicking the cell culture environment, contains randomly distributed phosphor-embedded beads and is placed at the bottom of the well. Water is added to the well, up to the opening that will be later sealed by a cover glass to eliminate the image distortion caused by the surface curvature at the water-air interface. As Figure 3.6 (b) depicted, when nitrogen is pumped through the channel beneath the well, oxygen will be depleted in the gel layer in the vicinity of the channel setting up a millimeter-scale oxygen gradient ranging from oxygen-depleted to air-equilibrated levels within the agarose gel sample.

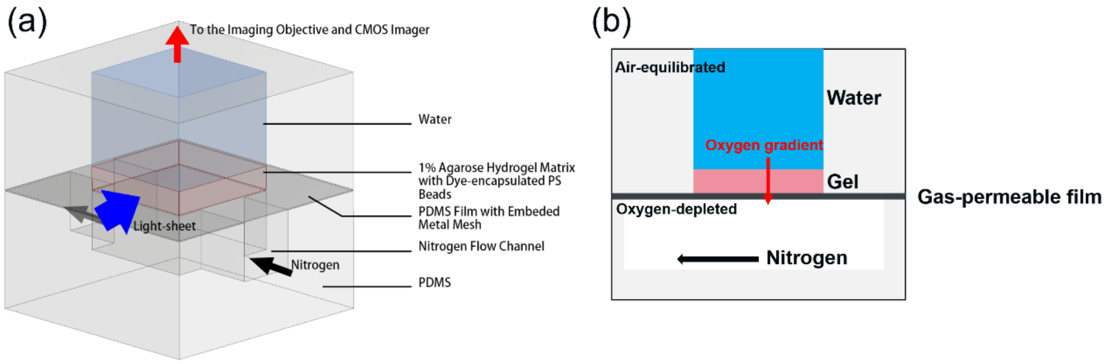

Figure 3.6 (a) The 3D model of the PDMS fluidic device for creating oxygen gradients in hydrogel samples. The directions of the light-sheet illumination and the signal detection are presented. (b) The schematic diagram of the generation of artificial oxygen gradient in the hydrogel layer.

As shown in Figure 3.6 (a), the light sheet can illuminate and excite the phosphor beads in a horizontal layer of the agarose gel, with the upward portion of the emission collected by the detection arm. By synchronously adjusting the position of the cubic sample and the focal plane of the imaging objective using a pair of manual translational stages, the emission from the probes at different depths can be examined. This enables the measurement of oxygen concentration at arbitrary locations within the hydrogel sample if the phosphor bead is properly positioned.

3.6 Image Acquisition and Data Processing Software

The Alvium 1800U 501m NIR camera (Allied Vision) in the optical setup for image acquisition is driven by the Python script that utilizes Vimba SDK (software suite for machine vision and CSI-2 cameras, Allied Vision). To achieve an optimized frame rate (60 Hz) and the fastest rolling shutter scanning speed

(7 μs/row), the camera is set in free-run mode, continuously streaming raw pixel data into the buffer during the experiment. The acquisition process involves capturing the data from the buffer and writing it to the hard drive as image files through the script. The script is designed to synchronize the light-sheet illumination with the acquisition process, allowing control over the illumination period and the number of consecutive frames being generated for each capture. The synchronized and limited exposure not only dramatically reduces the phototoxicity to the culture, but also minimizes the thermal influence on the luminescence lifetime. A 146 μs pixel exposure time was chosen to conduct low-pass integration filtering on the high-frequency components in the square wave-modulated signals since the low-cost laser diode illumination system can only accept transistor-transistor logic (TTL) control.

The data analysis is performed using MATLAB (MathWorks) programs. A graphical user interface (GUI) program based on MATLAB App Designer (MathWorks) has been developed to enable manual selection of regions of interest (ROIs) in the acquired images and display the corresponding fringes for fast assessment (See Figure 3.7). Additionally, a separate script has been written to implement least-square sinusoidal curve regression over the ROIs and extract the phase shift between the excitation and emission signals. The curve regression script also allows for assigning the number of consecutive frames to conduct averaging of the phase shift over the selected ROIs. At least 3 modulation cycles were included in the regions of interest (ROIs) for accurate extraction, corresponding to 100-120 rows in ROI heights. Meanwhile, the readouts on the same row were summed up to increase the signal-to-noise ratio, corresponding to 90-200 pixels in ROI widths which also depended on the light spot sizes.

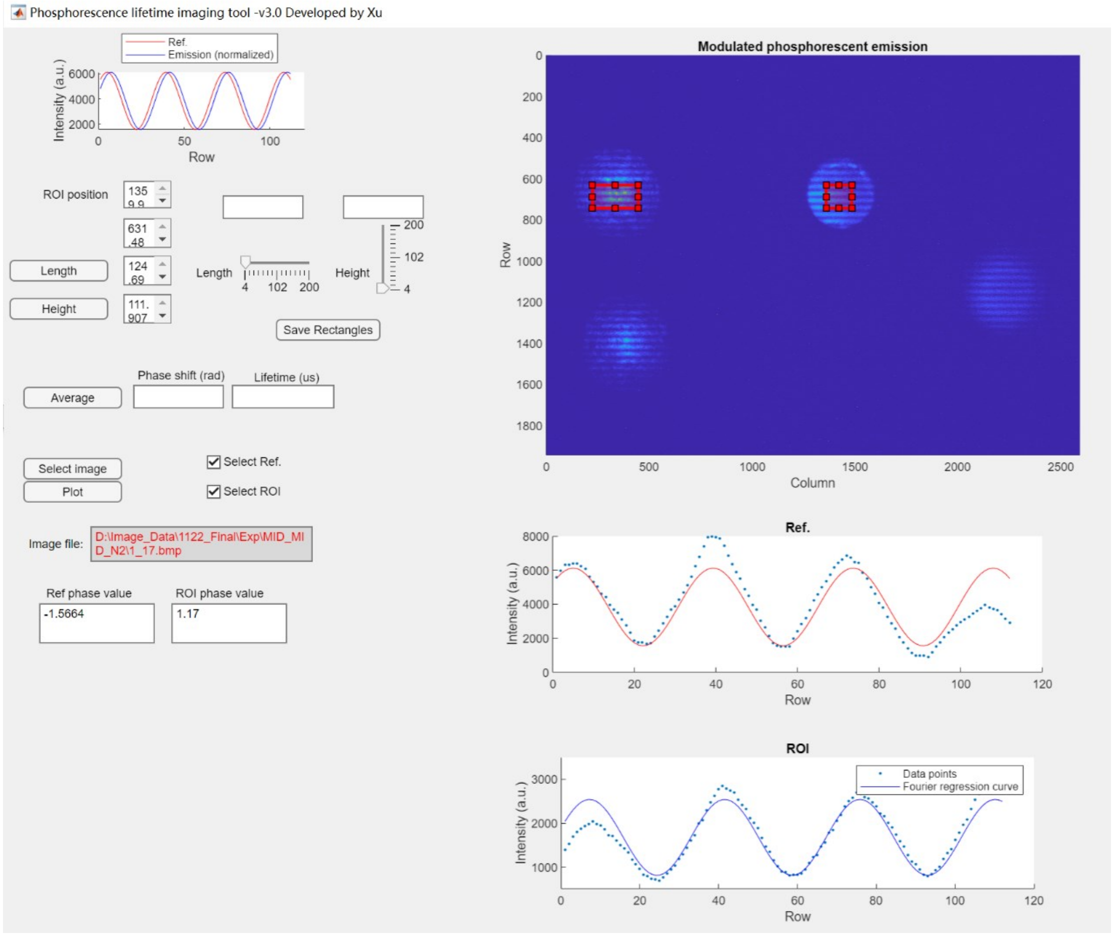

ROI position: 1359.9; 631.48; 124.69; 111.907

☑ Select Ref.

☑ Select ROI

Image file: D:\Image_Data\1122_Final\Exp\MID_MID_N2\1_17.bmp

Ref phase value: -1.5664

ROI phase value: 1.17

Figure 3.7 GUI of the phosphorescence lifetime imaging tool based on MATLAB. The region of interest squares (red rectangles) can be manually set across the image and fine tuned by the scrollbars or the input windows on the left side. The scatter plots of both the reference and ROI regions will be plotted, along with the Fourier regression curves. A preview plot of the phase difference between the two intensity-normalized regressed sinusoidal curves will also be presented on the top left side of the GUI.

Chapter 4: Results and Discussion

In order to verify the functionalities of the proposed low-cost 3D phosphorescence lifetime measurement system, experiments need to be designed on the aspect of spatial and temporal resolutions, reproducibility, and finally the viability of live cells throughout the measuring procedure. In this chapter, an averaging strategy will be introduced in section 4.1, compensating the phosphorescence lifetime measurement systematic error originating from the nonuniformity of the intensity distribution on the image. Secondly, experiments assessing the system’s reproducibility under constant environmental conditions will be introduced in section 4.2. Finally, system performance assessment based on a oxygen-gradient-generating fluidic device will be presented in section 4.3, validating the sub-millimeter spatial resolution and sub-microsecond temporal resolution.

4.1 Precise Phosphorescence Lifetime Determination from Spherical Polymer Beads Dispersed in the Hydrogel Model

Owing to light scattering and attenuation in the sample and the characteristics of the optical fiber, the brightness within the regions of interest (ROIs) is non-uniform and is related to the sample’s physical geometry, as Figure 4.1 (a) shows. This non-uniformity can affect the accuracy of the phase extraction process, which relies on all the readouts within a region to resolve the intrinsic modulated sinusoids. When the signal amplitude at each pixel varies, the weight of each data point will differ during the regression process, resulting in deviations of the calculated phase shift from the true value between the excitation and emission sinusoids. As shown in Figure 4.1 (b), since the phases of the intrinsic sinusoids proceed a certain step when the new frame is captured by the camera, the distortions on the sinusoidal signals are different in the two consecutive frames, leading to varied curve regression results. Those image brightness “envelopes”, which are due to the complicated light scattering along the optical paths and various geometries of the samples, are difficult to predict apriori and can potentially limit the use of lifetime measurement utilizing the rolling shutter effect in real applications, where the sample geometries can vary and be restricted by other technical considerations.

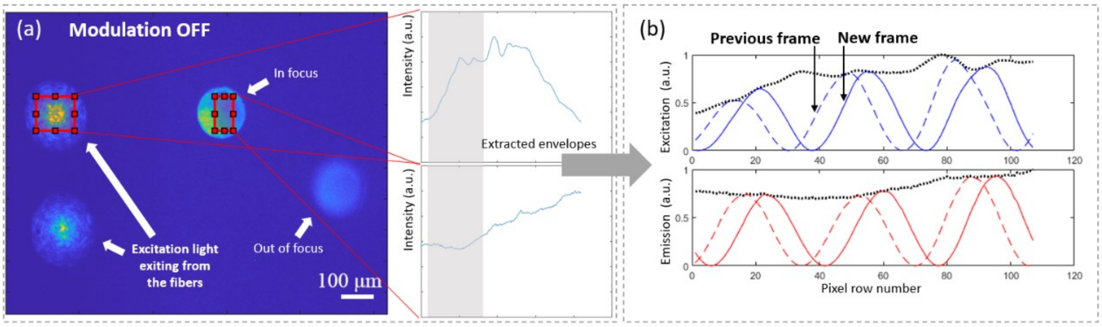

Figure 4.1 Demonstration of envelop-affected signal detection. (a) Non-uniformity in the image brightness in normal constant illumination. “Envelope” patterns from the two regions of interest (excitation and emission, respectively) are extracted and plotted along the row number. (b) Difference in the distortion of the modulated signals between the consecutive frames due to the non-uniformity in the image brightness (envelopes extracted from the gray areas). Since the consecutive frames are captured at different time points, the intrinsic modulation will undergo a phase increment, resulting in differently distorted fringe patterns extracted from the two frames over the same ROIs.

Figure 4.2 shows the phase shift values extracted from 800 successive frames captured at 68.125 fps from a polymer bead (probe) placed in an environment where the oxygen concentration was gradually decreasing. While the overall trend of increasing phase shift can be observed, the wide dispersion of the data points made it difficult to resolve minor variations in the phase shift accurately.

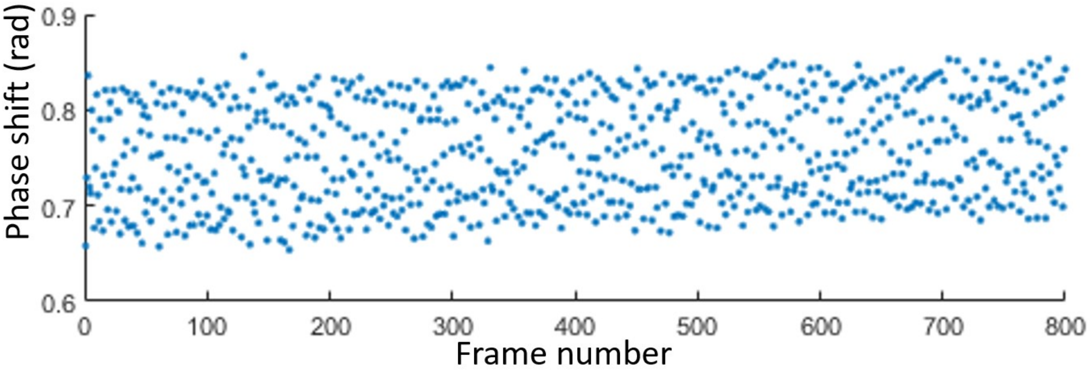

Figure 4.2 Phosphorescence emission phase shift values with respect to the excitation modulation from a fixed probe extracted from 800 successive frames captured at 68.125 fps. The values are plotted against the frame index, showing an ascending trend while the oxygen level around the probe is decreasing.

However, further data inspection reveals that this data dispersion is resulted from systematic error instead of random noise, and proper averaging strategy can solve this issue. As illustrated in Figure 4.3, given that the intrinsic modulated signal underwent approximately 2π for every 8 frames when the camera was freely running at 68.125 fps, with only a slight variation relative to the initial phase recorded 7 frames earlier, we can collect every 8th frame into a separate group. This yielded 7 groups of sinusoid-like sequences out of the scattered point set. The continuous pattern was foreseeable since each rearranged sequence was equivalent to the outcome of a virtual image-capturing process where the phase changes of the intrinsic signals between successive frames were minimal, unlike the large increments shown in Figure 4.2. The patterns indicate that there were underlying mechanisms in the distributions of the signal as shown in Fig. 4.3.

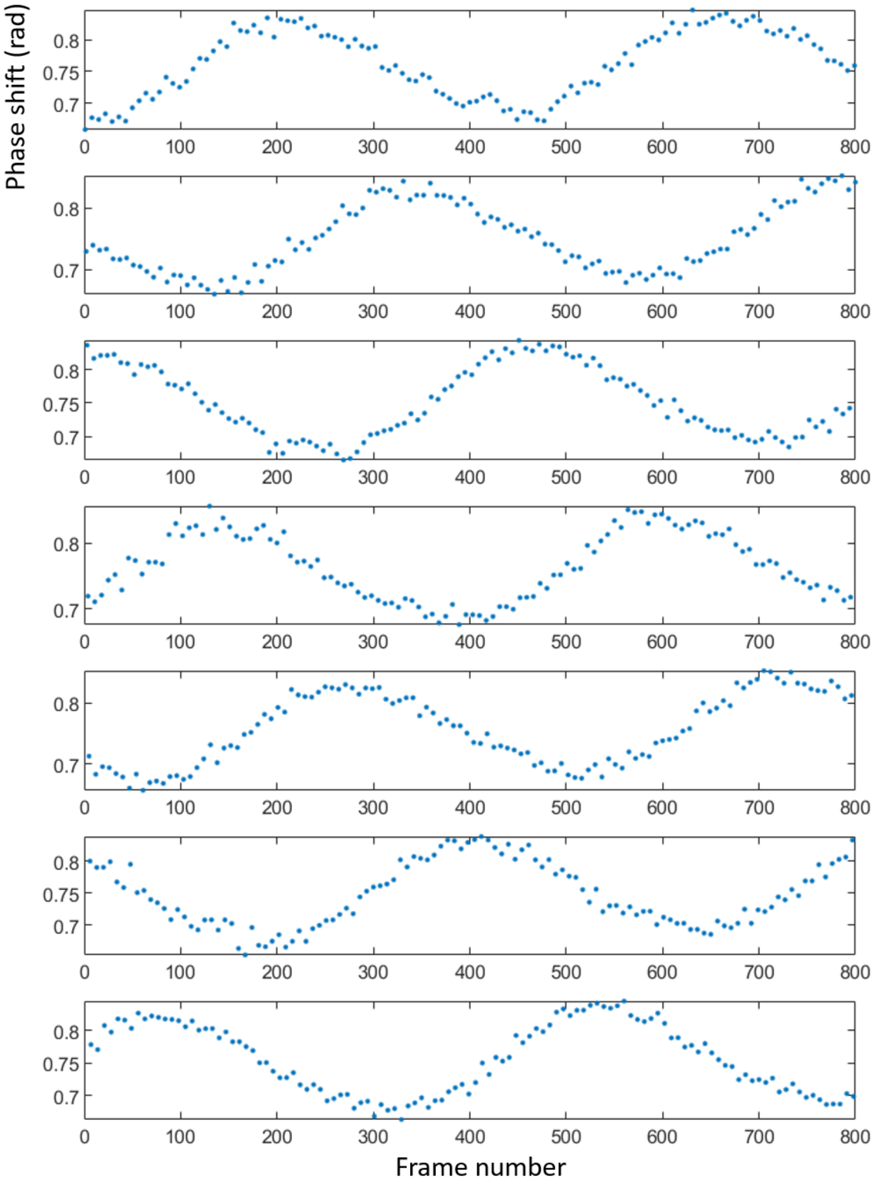

Figure 4.3 800 data points in Figure 4.2 are assorted by putting every 8th frame into one group while maintaining the original order. Each of the groups exhibits a similar sinusoid-like pattern.

To evaluate the scattering patterns of the calculated phase shift value sequence, we conducted a fringe pattern simulation that combined the envelopes extracted from Figure 4.1 with a pair of ideal sinusoids with preset phase difference which mimicked the ideal phase changes between the modulated excitation and the corresponding phosphorescence emission. In Figure 4.4, the simulated phase shifts, between randomly enveloped sinusoidal signals, calculated using the previous regression method are plotted against the initial phases of the intrinsic sinusoids from 0 to 2π, with the preset phase shift at 0.7 rad. It is evident that the curve is sinusoid-like regardless of changes in the envelopes, but the troughs and the crests are usually not symmetric. However, the integral mean of this curve aligns well with the preset phase shift value regardless of the random envelopes caused by non-uniform intensity distributions shown in Figure 4.1, which also holds for other values besides 0.7 rad. This suggests an averaging strategy can be applied to stabilize the measurement of emission phase shift, yet the mathematically rigorous proof still needs to be explored.

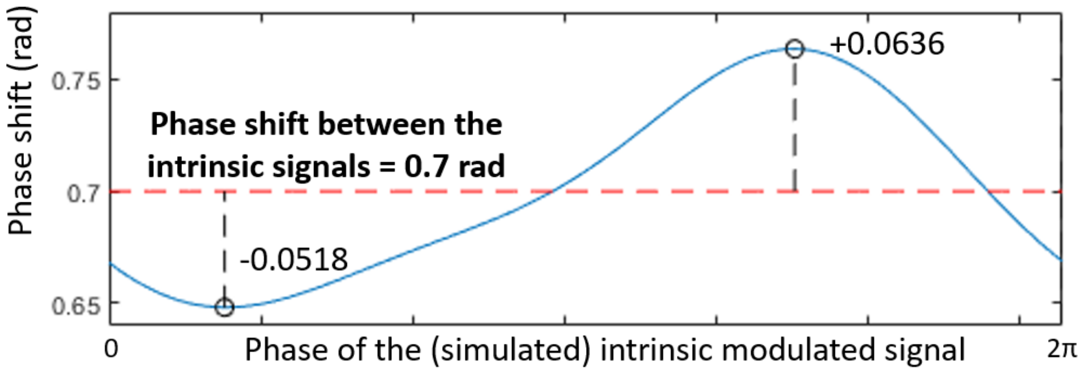

Figure 4.4 Simulated phase shift extraction results by applying least square regression on the real brightness envelop-modified ideal sinusoid pair with a preset phase difference (0.7 rad is specified only as a demonstration).

Picking 50 successive data points (frame 50-99) from Figure 4.2, we estimated the relative phase of each point's corresponding intrinsic signals according to the rearranged subsets and replotted these 50 points over a 2π span based on the estimation, as shown in Figure 4.5. It is akin to stitching 7 data point patches (each patch was assigned a unique color in the figure) from each of the subsets. The resulting data distribution has a sinusoid-like shape consistent with the curve we obtained from the simulation, with an average of 0.7538 rad, corresponding to the lifetime at 37.35 μs. As the extracted phase shift values from the 50-frame cluster can uniformly sample the curve shown in Figure 4.4 over the whole span, it proved that an averaging strategy of taking 50 frames for a phase shift measurement can closely estimate the true intrinsic phase shift value and eliminate the "envelope" effect caused by the brightness non-uniformity in the captured image.

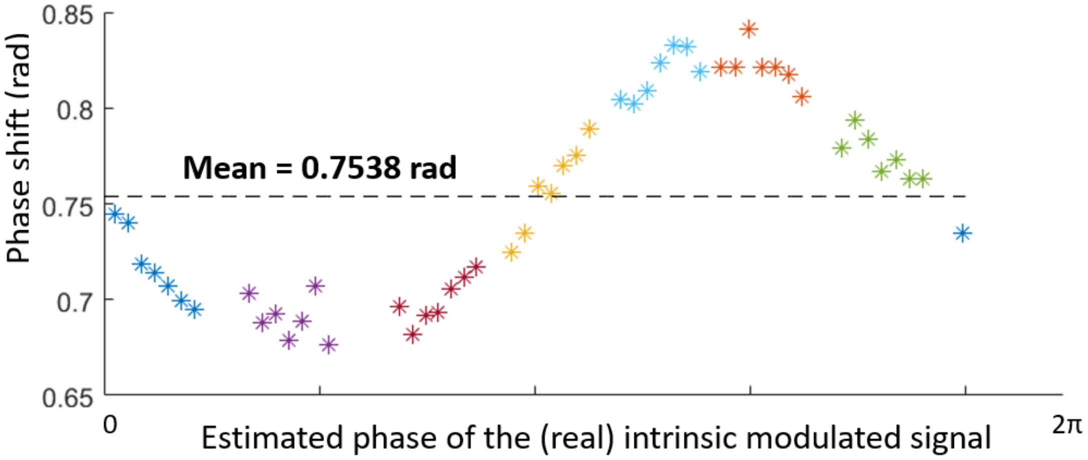

Figure 4.5 Rearranged 50 successive data points according to their relative positions on the sinusoid-like phase shift-phase of modulation curve estimated from the patterns of 7 rearranged point groups.

When a CMOS camera with a different rolling shutter scanning speed and frame rate is used, the frame cluster size for the averaging process can be determined by the coupling between the free-running image capture and the signal modulation. A similar rearrangement of the scattered data point set into several subsets with continuous patterns, as in Figure 4.3, should be obtained through experiments. This is because that the frame spacing of a conventional free-run camera streaming is in millisecond-level, while the period of the modulation is 250 μs for 4 kHz. As such, usually no specification would indicate the exact frame numbers whose corresponding phase elapsed in the modulation is the multiple of 2π. The minimal number of frames to conduct the average strategy is equivalent to the amount needed to reconstruct the sinusoid-like curve, as Figure 4.5 shows.

4.2 Assessing the Consistency of the Lifetime Measurement with Constant Environmental Conditions

The brightness non-uniformity in the image makes the phase shift values extracted from the individual frames differ from each other. By utilizing the average strategy proposed in the previous section, this lifetime measurement technique can closely approximate the true value distorted by the brightness “envelope”. However, the “envelope” itself has temporal variations at a larger timescale compared to the second-long capture process of a frame cluster, i.e., the brightness distribution within the ROI can change during the long experiment procedure even in the absence of external interference. In practical scenarios, these changes may be attributed to fluctuations in illumination intensity or slight displacements of the probes within the soft cell culture matrix. To assess the long-duration lifetime measurement stability of this design and guarantee its reproducibility for the same measured quantity, we conducted an experiment of continuous phosphorescence lifetime monitoring on a single bead within an air-equilibrated 1% agarose hydrogel matrix over 1500 seconds. The 1% agarose in water solution was heated in a 1500W microwave oven for 25 seconds, poured into a plastic cuvette, mixed with dye-embedded PS beads, and cured for 15 minutes while fully exposed to air. The sample was installed onto the imaging system shown in section 3.4 and one bead within the matrix was selected for continuous monitoring. For every 5 seconds, a cluster of 50 consecutive frames was captured at 68.125 fps. While the camera was on standby, the illumination was turned off by a relay to prevent thermally induced lifetime changes.

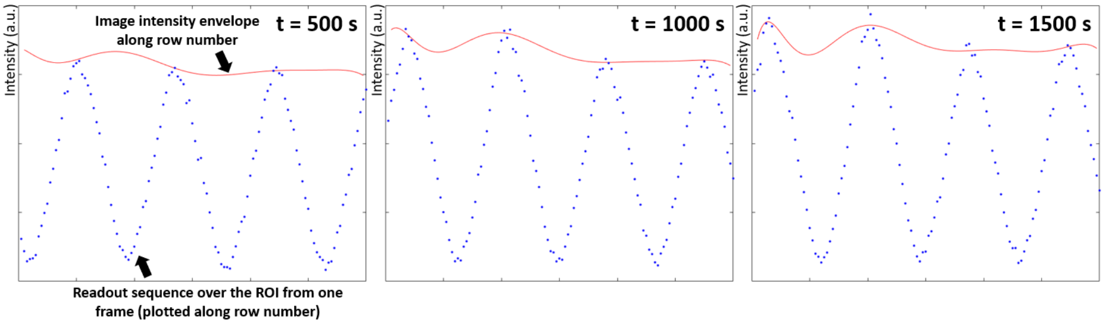

Figure 4.6 Pixel readout sequences over the same ROI (emission) at 500 s, 1000 s, and 1500 s. In each subfigure, data points were extracted from one single frame, with the envelope obtained from the neighboring 100 frames.

Figure 4.6 explicitly shows the brightness "envelope" changes in the phosphorescence emission during the experiment without any external disturbance. The amplitudes of the recorded signals exhibited an increasing trend from 500 s to 1500 s. All 15000 lifetime measurements from 300 50-frame clusters were plotted in Figure 4.7 along with the standard deviations of the lifetime values (right y-axis) within each frame cluster, indicating the width of the lifetime distribution of each cluster which relates to the "envelope" changes. It turned out that slight differences in the signal amplitudes can lead to large variations in the extracted phase shift values from individual frames.

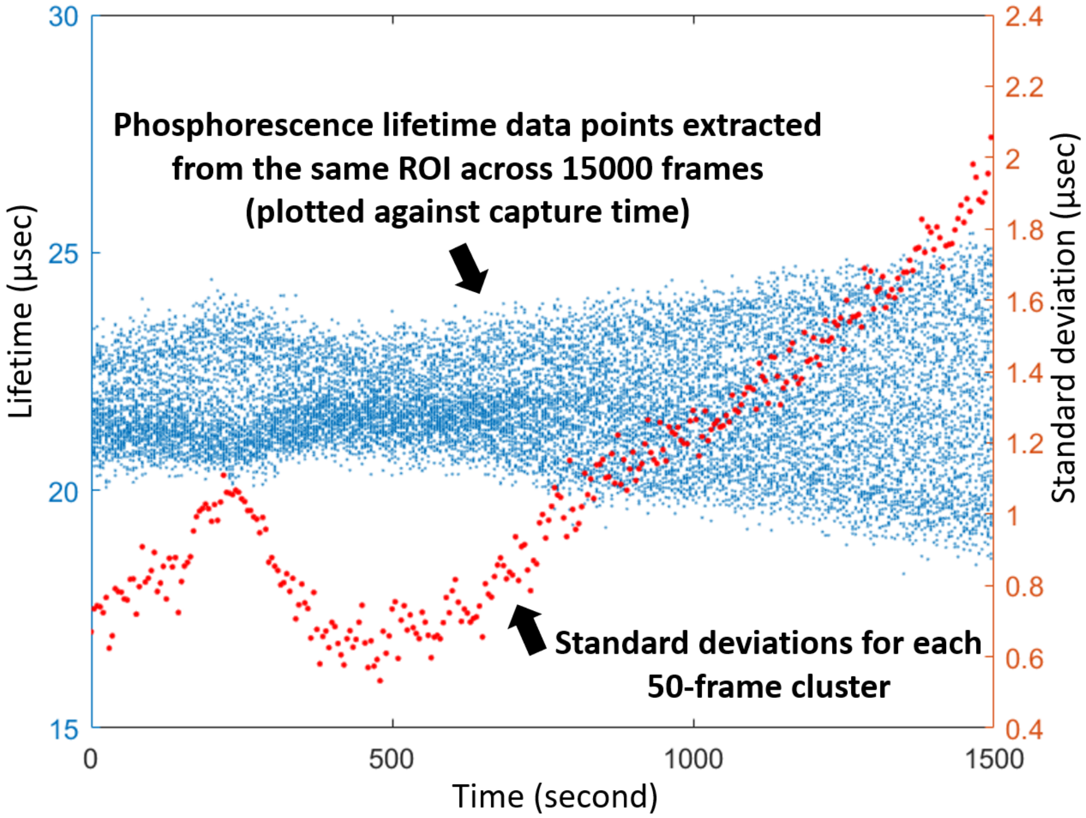

Figure 4.7 Phosphorescence lifetime monitoring results from a probe placed in agarose gel in a constant air-equilibrated condition for 1500 seconds. 50 successive frames were captured every 5 seconds. The standard deviations of the lifetime values within each cluster are plotted with respect to the right y-axis, indicating a gradual and continuous brightness envelope change in the captured image sequence.

Figure 4.8 (a) shows the corresponding averaged data points obtained from every cluster of 50 successive frames. Figure 4.8 (b) presents the distribution histogram of the 300 averaged data points, with over 90% of the measurement results lying within a 0.2 μs span. The experiment shows that profiling the continuously changing and highly arbitrary envelope is impractical and unnecessary. By applying the averaging strategy, we achieved a ±0.25 μs lifetime measurement error range, which corresponds to a ±0.2% of 1 atm pO_2 accuracy for monitoring oxygen concentration, over the entire 1500-second experiment under unchanged conditions with unpredictably changing image brightness. This analysis suggests the high-resolution measurement of the phosphorescence lifetime, and hence the oxygen concentration can be ensured over long durations of time in applications such as tissue engineering which require the culture of cells from hours to several days, over which the illumination conditions can change.

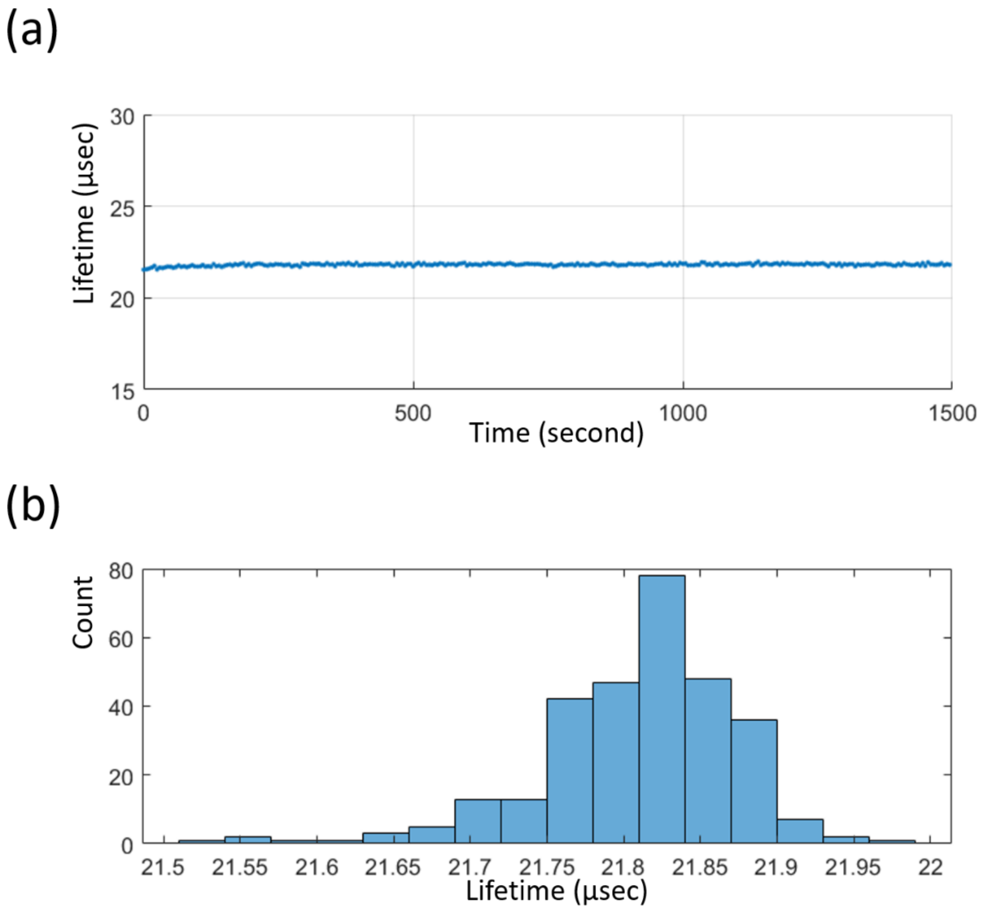

Figure 4.8 (a) Averaged lifetime values throughout the experiment duration according to the proposed averaging strategy. (b) Histogram of 300 lifetime values from the averaging results. 90% of the points lie in a 0.2 μs span, where the overall distribution is within 0.5 μs.

Additionally, by applying Eq. 2.3 and Eq. 3.5, we establish a relationship between the measured phase shift and the corresponding oxygen partial pressure:

$$pO_2 = \frac{1}{K_{SV}}\left(\frac{2\pi f_{mod}\tau_0}{\tan\varphi_{phase\ shift}} - 1\right) \tag{4.1}$$

To measure oxygen partial pressure below normoxic conditions, current accuracy in the phase shift measurement based on the rolling shutter scanning technique provides reduced error in environments with lower oxygen levels due to the inverse relationship between the two quantities. This theoretical evidence validates the efficacy of the design for tissue/cell culture applications, where passive oxygen diffusion from air maintains oxygen levels ranging from 18% to below 5% due to various cellular oxygen-consuming activities.

4.3 Resolving Artificial Oxygen Gradient in 3D Cell Culture Model

The primary objective of this design is to resolve phosphorescence lifetime in 3D for oxygen concentration mapping throughout the volume of tissue engineering samples. To evaluate the system performance of resolving small-scale oxygen gradient in 3D cell culture constructs, we deployed phosphorescent probes inside the agarose hydrogel matrix to mimic the examination of cell culture construct using this system. The dye-embedded PS beads were distributed inside an agarose gel layer that was fabricated by the same procedure in the previous section and placed on top of a PDMS fluidic channel as shown in Figure 3.6. The spatial positions above the channel of four of these beads were measured by tuning the focus of a microscope and their relative positions are shown in Figure 4.9.

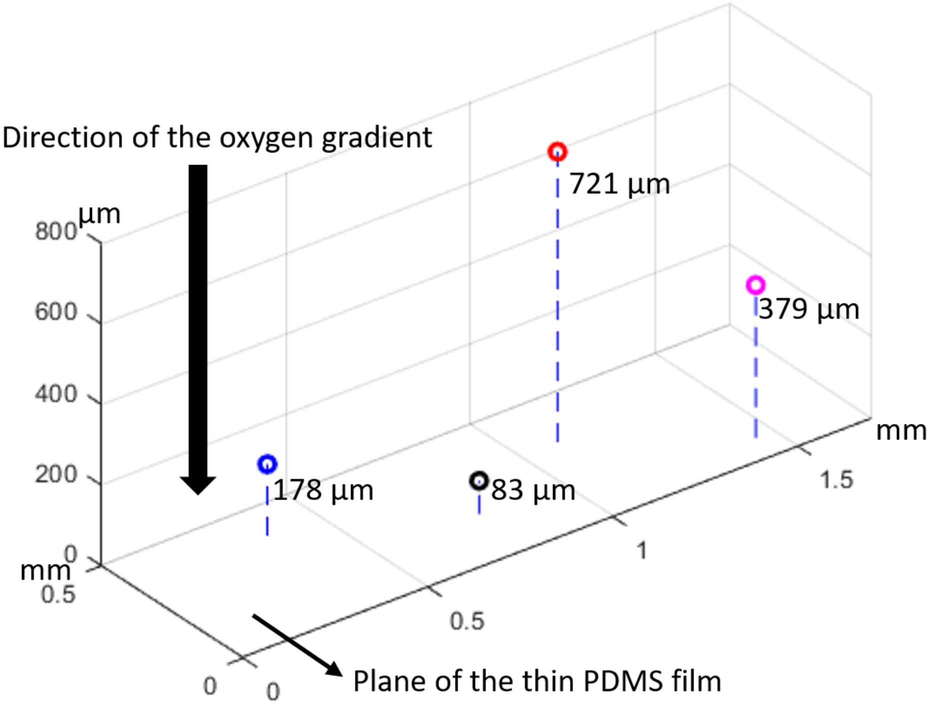

Figure 4.9 Relative positions of 4 phosphor beads within the agarose gel in an artificial downward oxygen gradient. Beneath the thin film is the nitrogen flow. Above the film is the agarose gel with dispersed phosphor beads.

Since the phosphorescence examination is conducted by tuning the manual translational stages, four separate imaging trials with 1500 seconds duration were conducted on each bead, with 1.5 hours for re-equilibration in between. The image capture and illumination were synchronized as described in section 4.2, with 50 consecutive frames captured every 5 seconds. Nitrogen was pumped through the hollow channel underneath the gel layer in the period indicated in Figure 4.10 (150 s - 600 s with respect to the start point), which diffuses nitrogen into the region in the gel in its vicinity and creates an oxygen gradient by passive oxygen diffusion through the gel layer. The continuous phosphorescence lifetime measurements performed on four of these beads are shown in Figure 4.10 and follow the change in oxygen concentration with time at these locations. The changes in the lifetime are negatively correlated to their distance from the channel as expected indicating that this method can be used to measure dynamic changes in oxygen concentration inside the bulk of hydrogels.

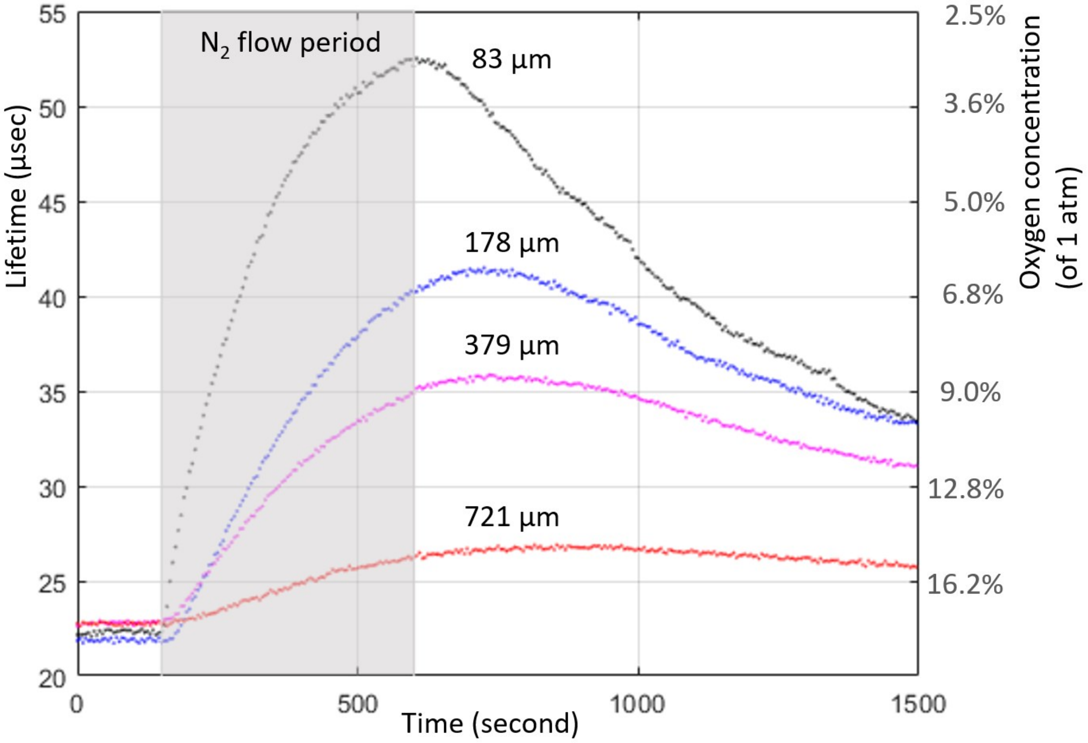

Figure 4.10 1500 seconds of lifetime monitoring of the emission from the 4 chosen phosphor beads at different heights above the thin gas-permeable film in the agarose gel sample. Nitrogen flow started at 150 seconds and ceased at 600 seconds. Oxygen concentration values corresponding to the lifetime values on the ticks are labeled on the right y-axis. Note that the concentration values are non-linear with respect to the axis ticks. Bead positions and the corresponding curves are drawn in different colors for distinction.

According to the linearity between the lifetime and the partial pressure described in Eq. 4.1, the Stern-Volmer constant can be estimated by two endpoints of the lifetime-oxygen partial pressure curve (21 µs - 21% pO_2, 70 µs – 0% pO_2) provided in [61]. As such, the right y-axis in Figure 4.10 shows the approximated oxygen partial pressure in percentages of 1 atm responding to the ticks on the left lifetime axis. Since these phosphorescence probes were positioned within a span of 0.5mm×1.5mm×700µm, it suggests that this design can achieve sub-millimeter spatial resolution, making it compatible with the requirements for oxygen concentration monitoring of a broad range of tissue engineering research. It also indicates a high dynamic range (45 µs-70 µs) when measuring low oxygen levels (below 5% of 1 atm) based on phosphorescence lifetime, providing excellent resolution in terms of the oxygen concentration and the potential of implementation in hypoxia-related culture experiments as described by Eq. 4.1.

Although each curve is internally consistent with an error range of ±0.25 µs, their initial lifetime under the same conditions can differ by up to 1 µs from one another, which can be observed in Figure 4.10. This variation is attributable to differences in particle sizes, which result in distinct gas diffusion rates and the consequent varying degrees of phosphorescence quenching inside the beads. To address this issue, potential improvements could involve using smaller diameter beads and implementing more precise particle synthesis techniques.

Since 3D cultures are increasingly used as tissue surrogates, it is crucial to assess whether 3D culture protocols can provide an adequate oxygen level for studying physiopathological processes [73]. Many culture designs rely on millimeter-sized cubic hydrogel constructs, where oxygen is passively diffused from the atmosphere. Oxygen permeability has been engineered [74] or extensively examined in the hydrogel matrix [27, 75] for improved manipulation of tissue samples. However, these attempts have proven to be still costly [76, 77] or have resulted in insufficient 3D information [78]. In this regard, our system evaluation experiment, which incorporates an artificial oxygen gradient, demonstrates significant potential for implementing a cost-effective and viable 3D oxygen level measurement design in such applications. For future investigations on oxygen distribution or pericellular oxygen tension monitoring in real cell culture scenarios, it is necessary to explore specific methods and patterns for deploying phosphor beads in conjunction with the construct designs. For instance, employing a 3D probe array with equally spaced individual beads would be more advantageous than the random bead distribution proposed in this section, as it would enable a more rigorous mapping of oxygen levels in the 3D environment.

Chapter 5: Conclusion and Future Work

5.1 Conclusion

Oxygen concentration is a crucial factor in cell viability and metabolic activities for both *in vivo* and cell culture environments. Therefore, monitoring oxygen levels is a vital aspect of tissue engineering research. However, accurate measurement of oxygen concentrations in 3D typically requires expensive and complex instrumentation to quantify phosphorescence lifetime, which can be a barrier for research groups with a biological or clinical background. To address this issue, a low-cost design for conducting 3D phosphorescence lifetime imaging inside hydrogel samples to accurately measure oxygen concentrations has been proposed, implemented, and evaluated in this thesis. Building on the combination of a customized light-sheet microscope system and the rolling-shutter image capturing, the proposed luminescence lifetime imaging system is competitive with existing solutions that use either integrated advanced imaging systems with photon-counting devices or customized single-point detection, but it comes at a significantly lower cost while maintaining satisfactory performance. With a temporal precision of ±0.25 μs owing to the improved lifetime determination algorithm, the proposed design can resolve sub-millimeter oxygen gradients, achieve a ±0.2% of 1 atm pO_2 accuracy for monitoring oxygen concentration, and be adaptable to a broad range of sample geometries. This makes it a suitable option for peer researchers to quickly implement 3D oxygen concentration monitoring with dramatically reduced barriers to entry.

Although this thesis presents a cost-effective method for precisely measuring 3D oxygen concentration within cell culture samples, further improvements are still required to its robust integration into the cell culture research community. Specifically, the current image capture process could be upgraded to incorporate automatic light-sheet scanning and a corresponding algorithm to reconstruct oxygen distribution. Further, comprehensive cell viability tests should be conducted, and measures to mitigate phototoxicity resulting from light-sheet illumination during the imaging procedure need to be implemented.

5.2 Future Work

5.2.1 Automatic Light-Sheet Scanning

As shown in Figure 3.4, the light-sheet illumination scans through the sample volume by manually adjusting the translation stage holding the sample. While this configuration allows for the examination of oxygen concentration at specific locations within the sample, achieving accurate and timely volumetric oxygen distribution mapping through manual translation proves impractical for studies focusing on oxygen diffusion.

To address this limitation, motorized translation stages can be integrated into both the sample holder and the imaging arm. This adaptation is crucial as the objective focus changes with the longitudinal movement of the sample. Additionally, the implementation of auto-focusing algorithms becomes essential to ensure synchronized image capture throughout the light-sheet scanning process.

5.2.2 Cell Viability Test

The light-sheet illumination employs a 405 nm laser, which is reported to be much more photo-toxic to cells than lower energy light [79]. Given the strong correlation between oxygen concentration and cellular metabolism, the need for continuous oxygen monitoring throughout the experiment, potentially spanning its entire duration, arises. Consequently, it becomes imperative to employ excitation light dose engineering to mitigate phototoxicity. In this thesis, the light is activated only when the camera is operational, limiting the sample's exposure to excitation light to one-tenth of the overall time. Despite this reduction, it remains a significant duration compared to commercially available confocal laser scanning systems. To further minimize exposure, synchronization of the light-sheet illumination with the image capture trigger can be imposed. Additionally, an improved optical design, featuring a smaller dimension for the light-sheet, is favored to alleviate cell stress during exposure.

LIST OF REFERENCES

1. R. J. Fleischaker and A. J. Sinskey, "Oxygen demand and supply in cell culture," European journal of applied microbiology and biotechnology **12**, 193-197 (1981).

2. A. T. Nahapetian, J. N. Thomas, and W. G. Thilly, "Optimization of environment for high density Vero cell culture: effect of dissolved oxygen and nutrient supply on cell growth and changes in metabolites," J Cell Sci **81**, 65-103 (1986).

3. C. Sieblist, M. Jenzsch, M. Pohlscheidt, and A. Lübbert, "Insights into large-scale cell-culture reactors: I. Liquid mixing and oxygen supply," Biotechnology Journal **6**, 1532-1546 (2011).

4. H. E. Abaci, R. Devendra, Q. Smith, S. Gerecht, and G. Drazer, "Design and development of microbioreactors for long-term cell culture in controlled oxygen microenvironments," Biomedical Microdevices **14**, 145-152 (2012).

5. K. Parmar, P. Mauch, J.-A. Vergilio, R. Sackstein, and J. D. Down, "Distribution of hematopoietic stem cells in the bone marrow according to regional hypoxia," Proceedings of the National Academy of Sciences **104**, 5431-5436 (2007).

6. B. Muz, P. de la Puente, F. Azab, and A. K. Azab, "The role of hypoxia in cancer progression, angiogenesis, metastasis, and resistance to therapy," Hypoxia (Auckl) **3**, 83-92 (2015).

7. D. Shweiki, M. Neeman, A. Itin, and E. Keshet, "Induction of vascular endothelial growth factor expression by hypoxia and by glucose deficiency in multicell spheroids: implications for tumor angiogenesis," Proceedings of the National Academy of Sciences **92**, 768-772 (1995).

8. G. Mehta, K. Mehta, D. Sud, J. W. Song, T. Bersano-Begey, N. Futai, Y. S. Heo, M.-A. Mycek, J. J. Linderman, and S. Takayama, "Quantitative measurement and control of oxygen levels in microfluidic poly(dimethylsiloxane) bioreactors during cell culture," Biomedical Microdevices **9**, 123-134 (2007).

9. M. Yazdani, "Technical aspects of oxygen level regulation in primary cell cultures: A review," Interdiscip Toxicol **9**, 85-89 (2016).

10. S. M. Grist, K. L. Bennewith, and K. C. Cheung, "Oxygen Measurement in Microdevices," Annu Rev Anal Chem (Palo Alto Calif) **15**, 221-246 (2022).

11. S. M. Grist, L. Chrostowski, and K. C. Cheung, "Optical oxygen sensors for applications in microfluidic cell culture," Sensors (Basel) **10**, 9286-9316 (2010).

12. A. Shahin-Shamsabadi and P. R. Selvaganapathy, "A rapid biofabrication

technique for self-assembled collagen-based multicellular and heterogeneous 3D tissue constructs," Acta Biomater **92**, 172-183 (2019).

13. A. Shahin-Shamsabadi and P. R. Selvaganapathy, "Tissue-in-a-Tube: three-dimensional in vitro tissue constructs with integrated multimodal environmental stimulation," Mater Today Bio **7**, 100070 (2020).

14. O. S. Wolfbeis, "Luminescent sensing and imaging of oxygen: fierce competition to the Clark electrode," Bioessays **37**, 921-928 (2015).

15. R. L. Wilson, J. P. Connell, and K. J. Grande-Allen, "Monitoring Oxygen Levels within Large, Tissue-Engineered Constructs Using Porphyin-Hydrogel Microparticles," ACS Biomater Sci Eng **5**, 4522-4530 (2019).

16. J. A. Spencer, F. Ferraro, E. Roussakis, A. Klein, J. Wu, J. M. Runnels, W. Zaher, L. J. Mortensen, C. Alt, R. Turcotte, R. Yusuf, D. Cote, S. A. Vinogradov, D. T. Scadden, and C. P. Lin, "Direct measurement of local oxygen concentration in the bone marrow of live animals," Nature **508**, 269-273 (2014).

17. M. F. Wesseler, M. N. Johansen, A. Kiziltay, K. I. Mortensen, and N. B. Larsen, "Optical 4D oxygen mapping of microperfused tissue models with tunable <i>in vivo</i>-like 3D oxygen microenvironments," Lab Chip **22**, 4167-4179 (2022).

18. H. Kurokawa, H. Ito, M. Inoue, K. Tabata, Y. Sato, K. Yamagata, S. Kizaka-Kondoh, T. Kadonosono, S. Yano, M. Inoue, and T. Kamachi, "High resolution imaging of intracellular oxygen concentration by phosphorescence lifetime," Sci Rep **5**, 10657 (2015).

19. S. Kalinina, J. Breymayer, K. Reeß, L. Lilge, A. Mandel, and A. Rück, "Correlation of intracellular oxygen and cell metabolism by simultaneous PLIM of phosphorescent TLD1433 and FLIM of NAD(P)H," Journal of Biophotonics **11**, e201800085 (2018).

20. H. Choi, D. S. Tzeranis, J. W. Cha, P. Clémenceau, S. J. G. de Jong, L. K. van Geest, J. H. Moon, I. V. Yannas, and P. T. C. So, "3D-resolved fluorescence and phosphorescence lifetime imaging using temporal focusing wide-field two-photon excitation," Opt. Express **20**, 26219-26235 (2012).

21. E. J. Mahoney, H.-H. L. Hsu, F. Du, B. Xiong, P. R. Selvaganapathy, and Q. Fang, "Optofluidic Dissolved Oxygen Sensing With Sensitivity Enhancement Through Multiple Reflections," IEEE Sensors Journal **19**, 10452-10460 (2019).

22. B. Xiong, E. Mahoney, J. F. Lo, and Q. Fang, "A Frequency-domain optofluidic dissolved oxygen sensor with total internal reflection design for in situ monitoring," IEEE Journal of Selected Topics in Quantum Electronics, 1-1 (2020).

23. F. Wang, L. Chen, J. Zhu, X. Hu, and Y. Yang, "A Phosphorescence Quenching-Based Intelligent Dissolved Oxygen Sensor on an Optofluidic Platform," Micromachines (Basel) **12**(2021).

24. Y. Hirakawa, T. Yoshihara, M. Kamiya, I. Mimura, D. Fujikura, T. Masuda, R. Kikuchi, I. Takahashi, Y. Urano, S. Tobita, and M. Nangaku, "Quantitating intracellular oxygen tension in vivo by phosphorescence lifetime measurement," Sci Rep **5**, 17838 (2015).

25. R. Sen, L. M. Hirvonen, A. Zhdanov, P. Svihra, S. Andersson-Engels, A. Nomerotski, and D. Papkovsky, "New luminescence lifetime macro-imager based on a Tpx3Cam optical camera," Biomed Opt Express **11**, 77-88 (2020).

26. M. Moßhammer, V. V. Scholz, G. Holst, M. Kühl, and K. Koren, "Luminescence Lifetime Imaging of O2 with a Frequency-Domain-Based Camera System," J Vis Exp (2019).

27. S. C. Lesher-Perez, G. A. Kim, C. H. Kuo, B. M. Leung, S. Mong, T. Kojima, C. Moraes, M. D. Thouless, G. D. Luker, and S. Takayama, "Dispersible oxygen microsensors map oxygen gradients in three-dimensional cell cultures," Biomater Sci **5**, 2106-2113 (2017).

28. A. C. Mitchell, J. E. Wall, J. G. Murray, and C. G. Morgan, "Direct modulation of the effective sensitivity of a CCD detector: a new approach to time-resolved fluorescence imaging," J Microsc **206**, 225-232 (2002).

29. A. C. Mitchell, J. E. Wall, J. G. Murray, and C. G. Morgan, "Measurement of nanosecond time-resolved fluorescence with a directly gated interline CCD camera," J Microsc **206**, 233-238 (2002).

30. L. M. Hirvonen, F. Festy, and K. Suhling, "Wide-field time-correlated single-photon counting (TCSPC) lifetime microscopy with microsecond time resolution," Opt Lett **39**, 5602-5605 (2014).

31. L. M. Hirvonen, Z. Petrášek, A. Beeby, and K. Suhling, "Sub-μs time resolution in wide-field time-correlated single photon counting microscopy obtained from the photon event phosphor decay," New Journal of Physics **17**(2015).

32. M. Tebyetekerwa, J. Zhang, Z. Xu, T. N. Truong, Z. Yin, Y. Lu, S. Ramakrishna, D. Macdonald, and H. T. Nguyen, "Mechanisms and Applications of Steady-State Photoluminescence Spectroscopy in Two-Dimensional Transition-Metal Dichalcogenides," ACS Nano **14**, 14579-14604 (2020).

33. J. Lakowicz, *Principles of Fluorescence Spectroscopy* (2006), Vol. 1.

34. I. Isenberg and R. D. Dyson, "The analysis of fluorescence decay by a method of moments," Biophysical Journal **9**, 1337-1350 (1969).

35. H. Kautsky, "Quenching of luminescence by oxygen," Transactions of the Faraday Society **35**, 216-219 (1939).

36. J. R. Lakowicz and G. Weber, "Quenching of fluorescence by oxygen. A probe for structural fluctuations in macromolecules," Biochemistry **12**, 4161-4170 (1973).

37. Y. Feng, J. Cheng, L. Zhou, X. Zhou, and H. Xiang, "Ratiometric optical oxygen sensing: a review in respect of material design," Analyst **137**, 4885-4901 (2012).

38. X.-H. Wang, H.-S. Peng, H. Ding, F.-T. You, S.-H. Huang, F. Teng, B. Dong, and H.-W. Song, "Biocompatible fluorescent core–shell nanoparticles for ratiometric oxygen sensing," Journal of Materials Chemistry **22**(2012).

39. X. Y. Dong, Y. Si, J. S. Yang, C. Zhang, Z. Han, P. Luo, Z. Y. Wang, S. Q. Zang, and T. C. W. Mak, "Ligand engineering to achieve enhanced ratiometric oxygen sensing in a silver cluster-based metal-organic framework," Nat Commun **11**, 3678 (2020).

40. J. Alderman, J. Hynes, S. M. Floyd, J. Kruger, R. O'Connor, and D. B. Papkovsky, "A low-volume platform for cell-respirometric screening based on quenched-luminescence oxygen sensing," Biosens Bioelectron **19**, 1529-1535 (2004).

41. W. Becker, A. Bergmann, M. A. Hink, K. Konig, K. Benndorf, and C. Biskup, "Fluorescence lifetime imaging by time-correlated single-photon counting," Microsc Res Tech **63**, 58-66 (2004).

42. E. L. Dereniak, M. Gersbach, J. P. Hartke, R. Trimananda, Y. Maruyama, P. D. LeVan, A. K. Sood, M. Fishburn, D. Stoppa, R. E. Longshore, M. Razeghi, J. Richardson, R. Walker, R. K. Henderson, and E. Charbon, "High frame-rate TCSPC-FLIM using a novel SPAD-based image sensor," in *Detectors and Imaging Devices: Infrared, Focal Plane, Single Photon,* (2010).

43. L. Pancheri and D. Stoppa, "A SPAD-based pixel linear array for high-speed time-gated fluorescence lifetime imaging," in *2009 Proceedings of ESSCIRC*, (IEEE, 2009), 428-431.

44. K. R. Rivera, V. A. Pozdin, A. T. Young, P. D. Erb, N. A. Wisniewski, S. T. Magness, and M. Daniele, "Integrated phosphorescence-based photonic biosensor (iPOB) for monitoring oxygen levels in 3D cell culture systems," Biosens Bioelectron **123**, 131-140 (2019).

45. M. Mosshammer, V. V. Scholz, G. Holst, M. Kuhl, and K. Koren, "Luminescence Lifetime Imaging of O2 with a Frequency-Domain-Based Camera System," J Vis Exp (2019).

46. L. M. Hirvonen, F. Festy, and K. Suhling, "Wide-field time-correlated single-photon counting (TCSPC) lifetime microscopy with microsecond time resolution," Optics Letters **39**, 5602-5605 (2014).

47. Z. Petrášek and K. Suhling, "Photon arrival timing with sub-camera exposure time resolution in wide-field time-resolved photon counting imaging," Opt. Express **18**, 24888-24901 (2010).

48. L. Dinu, A. Eppink, F. Rosca-Pruna, H. Offerhaus, W. Van der Zande, and M. Vrakking, "Application of a time-resolved event counting technique in velocity map imaging," Review of Scientific Instruments **73**, 4206-4213 (2002).

49. D. Strasser, X. Urbain, H. Pedersen, N. Altstein, O. Heber, R. Wester, K. Bhushan, and D. Zajfman, "An innovative approach to multiparticle three-dimensional imaging," Review of Scientific Instruments **71**, 3092-3098 (2000).

50. A. Morimoito, T. Yatsuhashi, T. Shimada, L. Biczók, D. A. Tryk, and H. Inoue, "Radiationless Deactivation of an Intramolecular Charge Transfer Excited State through Hydrogen Bonding: Effect of Molecular Structure and Hard−Soft Anionic Character in the Excited State," The Journal of Physical Chemistry A **105**, 10488-10496 (2001).

51. M. Quaranta, S. M. Borisov, and I. Klimant, "Indicators for optical oxygen sensors," Bioanal Rev **4**, 115-157 (2012).

52. M. Bose, J. Hagerty, J. Boes, C. S. Kim, W. Stoecker, and P. Nam, "Optical Oxygen Sensor Patch Printed with Polystyrene Microparticles-based Ink on Flexible Substrate," IEEE Sens J **21**, 21494-21502 (2021).

53. E. Schmälzlin, J. T. van Dongen, I. Klimant, B. Marmodée, M. Steup, J. Fisahn, P. Geigenberger, and H. G. Löhmannsröben, "An optical multifrequency phase-modulation method using microbeads for measuring intracellular oxygen concentrations in plants," Biophys J **89**, 1339-1345 (2005).

54. S. Schreml, R. J. Meier, O. S. Wolfbeis, T. Maisch, R. M. Szeimies, M. Landthaler, J. Regensburger, F. Santarelli, I. Klimant, and P. Babilas, "2D luminescence imaging of physiological wound oxygenation," Exp Dermatol **20**, 550-554 (2011).

55. L. J. Gillespie, "The Gibbs-Dalton Law of Partial Pressures," Physical Review **36**, 121-131 (1930).

56. N. A. Gokcen, "APPLICATION OF GIBBS AND GIBBS—DUHEM EQUATIONS TO TERNARY AND MULTICOMPONENT SYSTEMS," The Journal of Physical Chemistry **64**, 401-406 (1960).

57. K. Koren, L. Hutter, B. Enko, A. Pein, S. M. Borisov, and I. Klimant, "Tuning the dynamic range and sensitivity of optical oxygen-sensors by employing differently substituted polystyrene-derivatives," Sens Actuators B Chem **176**, 344-350 (2013).

58. X. D. Wang and O. S. Wolfbeis, "Optical methods for sensing and imaging oxygen: materials, spectroscopies and applications," Chem Soc Rev **43**, 3666-3761 (2014).

59. D. B. Papkovsky, G. V. Ponomarev, W. Trettnak, and P. O'Leary, "Phosphorescent Complexes of Porphyrin Ketones: Optical Properties and Application to Oxygen Sensing," Analytical Chemistry **67**, 4112-4117 (1995).

60. S.-K. Lee and I. Okura, "Photostable Optical Oxygen Sensing Material: Platinum Tetrakis(pentafluorophenyl)porphyrin Immobilized in Polystyrene," Analytical Communications **34**, 185-188 (1997).

61. S. Grenoble, M. Gouterman, G. Khalil, J. Callis, and L. Dalton, "Pressure-sensitive paint (PSP): concentration quenching of platinum and magnesium porphyrin dyes in polymeric films," Journal of Luminescence **113**, 33-44 (2005).

62. K. Koren, M. Mosshammer, V. V. Scholz, S. M. Borisov, G. Holst, and M. Kuhl, "Luminescence Lifetime Imaging of Chemical Sensors-A Comparison between Time-Domain and Frequency-Domain Based Camera Systems," Anal Chem **91**, 3233-3238 (2019).

63. J. R. Lakowicz, *Principles of fluorescence spectroscopy* (Springer, 2006).

64. C. K. Liang, L. W. Chang, and H. H. Chen, "Analysis and compensation of rolling shutter effect," IEEE Trans Image Process **17**, 1323-1330 (2008).

65. J. Gu, Y. Hitomi, T. Mitsunaga, and S. Nayar, "Coded rolling shutter photography: Flexible space-time sampling," in *2010 IEEE International Conference on Computational Photography (ICCP)*, 2010), 1-8.

66. O. Saurer, K. Koser, J.-Y. Bouguet, and M. Pollefeys, "Rolling Shutter Stereo," in *2013 IEEE International Conference on Computer Vision,* (2013), pp. 465-472.

67. V. Rengarajan, A. N. Rajagopalan, and R. Aravind, "From Bows to Arrows: Rolling Shutter Rectification of Urban Scenes," in *2016 IEEE Conference on Computer Vision and Pattern Recognition (CVPR)*, 2016), 2773-2781.

68. B. Xiong and Q. Fang, "Luminescence lifetime imaging using a cellphone camera with an electronic rolling shutter," Optics Letters **45**(2019).

69. E. J. Gualda, T. Vale, P. Almada, J. A. Feijo, G. G. Martins, and N. Moreno, "OpenSpinMicroscopy: an open-source integrated microscopy platform," Nat Methods **10**, 599-600 (2013).

70. F. Pampaloni, N. Ansari, and E. H. Stelzer, "High-resolution deep imaging of live cellular spheroids with light-sheet-based fluorescence microscopy," Cell Tissue Res **352**, 161-177 (2013).

71. C. Greb, "Infinity Optical Systems: From infinity optics to the infinity port," Optik & Photonik **11**, 34-37 (2016).

72. G. T. Vladisavljevic, H. Shahmohamadi, D. B. Das, E. E. Ekanem, Z. Tauanov, and L. Sharma, "Glass capillary microfluidics for production of monodispersed poly (DL-lactic acid) and polycaprolactone microparticles: experiments and numerical simulations," J Colloid Interface Sci **418**, 163-170 (2014).

73. A. Colom, R. Galgoczy, I. Almendros, A. Xaubet, R. Farré, and J. Alcaraz, "Oxygen diffusion and consumption in extracellular matrix gels: Implications for designing three-dimensional cultures," Journal of Biomedical Materials Research Part A **102**, 2776-2784 (2014).

74. M. K. Lee, M. H. Rich, K. Baek, J. Lee, and H. Kong, "Bioinspired tuning of

hydrogel permeability-rigidity dependency for 3D cell culture," Sci Rep **5**, 8948 (2015).

75. L. Figueiredo, R. Pace, C. D'Arros, G. Rethore, J. Guicheux, C. Le Visage, and P. Weiss, "Assessing glucose and oxygen diffusion in hydrogels for the rational design of 3D stem cell scaffolds in regenerative medicine," J Tissue Eng Regen Med **12**, 1238-1246 (2018).

76. N. A. Hosny, D. A. Lee, and M. M. Knight, "Single photon counting fluorescence lifetime detection of pericellular oxygen concentrations," J Biomed Opt **17**, 016007 (2012).

77. K. Funamoto, I. K. Zervantonakis, Y. Liu, C. J. Ochs, C. Kim, and R. D. Kamm, "A novel microfluidic platform for high-resolution imaging of a three-dimensional cell culture under a controlled hypoxic environment," Lab Chip **12**, 4855-4863 (2012).

78. C. Schmitz, I. Pepelanova, C. Ude, and A. Lavrentieva, "Studies on oxygen availability and the creation of natural and artificial oxygen gradients in gelatin-methacryloyl hydrogel 3D cell culture," J Tissue Eng Regen Med **16**, 977-986 (2022).

79. C. Boudreau, T.-L. Wee, Y.-R. Duh, M. P. Couto, K. H. Ardakani, and C. M. Brown, "Excitation Light Dose Engineering to Reduce Photo-bleaching and Photo-toxicity," Scientific Reports **6**, 30892 (2016).